# JGR Solid Earth

**Key Points:**

- We quantitatively calculated the distributions of effective normal stress along a plate interface using hydraulic models in subduction zones
- Neither smectite dehydration nor the presence of a splay fault can generate a local decrease in effective normal stress at shallow regions
- A locally low effective normal stress is realized when permeability locally decreases, potentially responsible for shallow slow earthquakes

## Steady-State Effective Normal Stress in Subduction Zones Based on Hydraulic Models and Implications for Shallow Slow Earthquakes

**Shunya Kaneki**[1] [ID] **and Hiroyuki Noda**[1]

[1]Disaster Prevention Research Institute, Kyoto University, Uji, Japan

**Abstract** The spatial distribution of effective normal stress, $\sigma_e$, is essential for understanding the fault motion. Although Rice (1992, https://doi.org/10.1016/s0074-6142(08)62835-1) proposed a steady-state solution for a vertical strike-slip fault zone with constant fluid properties, models that are based on the concept by Rice (1992, https://doi.org/10.1016/s0074-6142(08)62835-1) and are applicable for other tectonic settings have not yet been developed. Such a model is particularly important in subduction zones because the relationship between low $\sigma_e$ and slow earthquakes is often discussed. To quantitatively examine the causes of a local decrease in $\sigma_e$ on a shallow region of the subduction zone, we performed model calculations that incorporated mechanisms characteristic to subduction zones. Our basic model, which considers the effect of smectite dehydration and the mechanical effect of subduction, yields results that are consistent with those reported by Rice (1992, https://doi.org/10.1016/s0074-6142(08)62835-1): the gradient of $\sigma_e$ remarkably decreases with the increase in depth, whereas the realistic fluid properties rule out nearly constant $\sigma_e$ at depth. We obtained a monotonic increase in $\sigma_e$ with the increase in depth for the physically sound solutions and failed to generate a local decrease in $\sigma_e$. The presence of a splay fault and fluid leakage though it cannot decrease $\sigma_e$ locally. We found that a local decrease in permeability decreased $\sigma_e$ locally around an impermeable zone and, thus, possibly led to the occurrence of shallow slow earthquakes. The water release caused by the dehydration reaction may not be the dominant factor, although smectite dehydration releases silica and promotes its precipitation.

**Plain Language Summary** The development and deployment of observation networks over the last two decades allowed for the investigation of "slow earthquakes," slower fault slip events than regular earthquakes. The occurrence of these slow earthquakes in subduction zones is often discussed in association with high pressure of pore fluid in rocks along a subduction plate interface, whereas the dominant mechanism responsible for the high pore pressure is enigmatic and still under debate. In this study, we tackled this issue by developing new, sophisticated hydraulic models that consider various process characteristics of subduction zones. Our results indicate that the clogging process of conduits can induce such a local increase in pore pressure and, thus, potentially allow for the occurrence of slow earthquakes, whereas the effect of the dehydration reaction of smectite is only modest, which has been considered as a candidate mechanism for the high pore pressure. Our new hydraulic models consider more realistic and complex mechanisms in subduction zones than the previous models and may be directly applicable to more realistic earthquake cycle simulations in the future, which can elucidate fault motion in the crust.

## 1. Introduction

Failure strength along a particular plane in a rock increases with the increase in effective normal stress acting on it, $\sigma_e$ (compressive stress normal to that plane $\sigma$ minus pore-fluid pressure $p$), in the brittle regime (e.g., Byerlee's law; Byerlee, 1978). Classically, there are two end-member hypotheses with respect to the depth dependence of the gradient of $\sigma_e$: (a) the gradient of $p$ is hydrostatic and $\sigma_e$ increases linearly with depth, or (b) the gradient of $p$ becomes close to that of $\sigma$ at depth and $\sigma_e$ approaches a model- and parameter-dependent asymptotic value. In the former, the pore pressure ratio $p/\sigma$ is constant at all depths. Townend and Zoback (2000) showed that the results of stress measurements in boreholes in intraplate continental crust are in agreement with Byerlee's law if $p$ is hydrostatic. The latter is sometimes observed in sedimentary basins (e.g., Suppe & Wittke, 1977). The almost constant $\sigma_e$ at depth is realized as a consequence of the one-dimensional model proposed by Rice (1992) (hereafter referred to as R1992), which explains the weak frictional strength of the San Andreas fault. R1992 modeled upward fluid flow through a vertical strike-slip fault zone based on the following assumptions: (a)

**Writing – original draft:** Shunya Kaneki, Hiroyuki Noda
**Writing – review & editing:** Shunya Kaneki, Hiroyuki Noda

fluids are supplied at a constant rate from the base of the seismogenic crust, (b) the fault zone acts as a fluid channel because it has significantly higher permeability than the surrounding host rock, (c) the permeability of the fault zone is a rapidly decreasing function of $\sigma_e$, and (d) the fluid properties are depth-independent constants. Note that R1992 made no assumption on $p$ at the seismogenic base. The R1992's model has been employed as a boundary condition in the earthquake cycle simulations in a strike-slip fault (e.g., Lapusta et al., 2000) and in a plate subduction zone (e.g., Liu & Rice, 2005). However, it is a model for a strike-slip fault with constant fluid properties, and its applicability to other tectonic settings has not been examined. Many other hydraulic modeling have been performed in various tectonic regions, especially in subduction zones (e.g., Bekins et al., 1995; Ellis et al., 2015; Fulton et al., 2009; Lauer & Saffer, 2012, 2015; Saffer & Bekins, 1998; Spinelli et al., 2006; Sun et al., 2020).

The recent development and deployment of seismic and geodetic observation networks have revealed that slow earthquakes, which are fault slip events with significantly slower slip rates or lower dominant frequency than regular earthquakes, occur in subduction zones worldwide (e.g., Obara, 2002; Rogers & Dragert, 2003; Hirose et al., 1999; for reviews, refer Beroza & Ide, 2011; Obara & Kato, 2016). The observations of these slow earthquakes have been interpreted as the presence of locally high $p$ and, thus, low $\sigma_e$ in their source regions (e.g., Kodaira et al., 2004; Shelly et al., 2006; Song et al., 2009). Earthquake cycle simulations employing locally low $\sigma_e$ as a boundary condition demonstrated the occurrence of aseismic transient slip events (Liu & Rice, 2007, 2009), suggesting the importance of the low $\sigma_e$ in the generation mechanism of the slow earthquakes. The local decrease in $\sigma_e$ can result from the local decrease in $\sigma$ and/or from the local increase in $p$. Regarding the former, for instance, Sun et al. (2020) demonstrated through a hydro-mechanical modeling that locally low $\sigma$ can be realized around the trailing edge of the subducting seamount. The potential mechanisms leading to the latter, which are the main target of the present study, include fluid release from subducting sediments (e.g., Hyndman & Peacock, 2003) and reduction in permeability (e.g., Sibson, 1992). Although these possibilities are often discussed for deep slow earthquakes that occur below a seismogenic zone (e.g., Audet & Bürgmann, 2014; Gosselin et al., 2020; Hyndman et al., 2015), similar considerations of shallow slow earthquakes that occur above the seismogenic zone have rarely been reported, despite their globally wide occurrence (e.g., Nishikawa et al., 2019; Outerbridge et al., 2010; Wallace & Beavan, 2010).

One of the possible processes accompanied by the fluid release at the shallow portion of the subduction zone is the transformation of smectite to illite. This reaction occurs within a temperature range of approximately 50–150°C (Freed & Peacor, 1989), which corresponds to a depth range of approximately 5–15 km (Hyndman et al., 1997). This depth range roughly correlates with the source region of shallow slow earthquakes in various subduction zones, such as the Nankai Trough and the Japan Trench (e.g., Nishikawa et al., 2019), the Hikurangi Trench (e.g., Wallace & Beavan, 2010), and the Costa Rican subduction margin (e.g., Outerbridge et al., 2010). Conversely, some previous studies suggest that slow earthquakes are not related to clay dehydration (e.g., Peacock, 2009; Saffer & Wallace, 2015). Peacock (2009) performed two-dimensional finite element heat transfer modeling in the Cascadia subduction margin and the Nankai Trough and argued that episodic tremor and slip does not coincide with a specific chemical reaction. Therefore, the role of smectite dehydration in the generation of shallow slow earthquakes remains controversial. Although previous studies have modeled fluid flow in the crust by considering the smectite-to-illite transition (e.g., Bekins et al., 1995; Bethke, 1986; Ellis et al., 2015; Lauer & Saffer, 2015; Saffer & Bekins, 1998; Spinelli et al., 2006), a quantitative assessment of the effect of smectite dehydration has not yet been reported.

Locally decreased $\sigma_e$ at a certain depth can also be explained by the existence of an impermeable zone, which locally reduces permeability. This mechanism, known as the fault-valve behavior (Sibson, 1992), can be effective when, for example, the dissolved silica is deposited as quartz veins that fill the cracks originally present in bulk rocks (e.g., Chester & Logan, 1986). Audet and Bürgmann (2014) analyzed the seismological structure of a forearc crust in various subduction zones and proposed that the reduction in permeability due to silica cementation can exert dominant control of the occurrence of episodic slow slip events at the deep portion. Gosselin et al. (2020) observed the evolution of the seismological structure of the Cascadia subduction margin and concluded that fault-valve behavior is likely to occur during episodic tremor and slip. Although these studies have provided qualitative explanations for deep slow earthquakes, both deep and shallow slow earthquakes need to be discussed quantitatively based on appropriate models.

In this study, we attempted to address the question "What can cause the local increase in $p$ and the resultant local decrease in $\sigma_e$ at the source region of shallow slow earthquakes?" by quantitatively evaluating the $\sigma_e$ distribution

along a subduction plate interface based on hydraulic models that consider the processes characteristic of subduction zones. First, we briefly introduce the R1992's model, on which the concept of our models is based. After describing the details of the models, their formulations, and parameterizations, we showed representative $\sigma_e$ distributions calculated based on our basic model that considers smectite dehydration, as well as the mechanical effect of subduction of sediments and realistic water properties. Then, we investigated the effects of water leakage through a splay fault and the local reduction in permeability. By comparing the $\sigma_e$ distributions obtained using different models, we discuss the potential causes of the locally low $\sigma_e$ and, thus, the occurrence of shallow slow earthquakes in subduction zones. Furthermore, we discuss the implications of our modeling results on seismological observations and earthquake cycle simulations.

## 2. Methods

### 2.1. Model Description and Formulation in Rice (1992)

In this subsection, we briefly summarized the model and formulation in R1992, on which the concept of our models is based. R1992 assumes that fluid flows only along a vertical strike-slip fault zone because of the lower permeability of the surrounding host rock. Therefore, the steady-state mass flux of the fluid along the fault zone must be the same at all depths. Assuming constant fluid density, $\rho_f$, and constant fluid viscosity, $\eta_f$, the volumetric fluid flux per unit area $q$ can be expressed by Darcy's law as follows:

$$q = -\frac{k}{\eta_f}\left(\frac{dp}{dz} + \rho_f g\right) = q^0, \tag{1}$$

where $z$ is the coordinate along a fault interface ($z = 0$ is the surface and the vertical upward is positive), $k$ is the permeability of the fault zone, $g$ is the gravitational acceleration, and $q^0$ is the value of $q$ at $z = 0$. R1992 also assumes that fault-normal compressive stress $\sigma$ is equivalent to the lithostatic pressure $\rho g(-z)$, where $\rho$ is the bulk rock density. Because $p = \sigma - \sigma_e$, it follows from Equation 1 that

$$\frac{d\sigma_e}{d(-z)} = (\rho - \rho_f)g - \frac{q^0\eta_f}{k}. \tag{2}$$

The first and second terms in the right-hand side of Equation 2 represent the gravity force accounting for the buoyancy and seepage force, respectively. $d\sigma_e/d(-z)$ is positive at $z = 0$, and decreases with depth as $k$ decreases. When $k$ is a rapidly decreasing function of $\sigma_e$, $d\sigma_e/d(-z)$ approaches zero at depth. R1992 further assumes that permeability can be approximated by a simple exponential function, $k = k^0 \exp(-\sigma_e/\sigma^*)$, where $k^0$ is the permeability at the surface ($z = 0$ and $\sigma_e = 0$) and $\sigma^*$ is the characteristic stress. This assumption allows for the integration of Equation 2 as follows:

$$\sigma_e = \sigma^* \ln\left\{\left[\frac{\eta_f q^0}{k_0(\rho - \rho_f)g} + \left(1 - \frac{\eta_f q^0}{k_0(\rho - \rho_f)g}\right)\exp\left(\frac{(\rho - \rho_f)gz}{\sigma^*}\right)\right]^{-1}\right\}. \tag{3}$$

At a great depth, $\sigma_e$ approaches $\sigma^* \ln\left[(k_0(\rho - \rho_f)g)/(\eta_f q^0)\right]$ as a consequence of the R1992's model. For an oblique fluid channel with a dip angle $\theta$, we have to replace only $g$ with $g\sin\theta$ in Equation 3.

### 2.2. Model Description and Formulation in This Study

Based on the R1992's model, we developed a hydraulic model that considers the effect of smectite dehydration, as well as the mechanical effect of subduction. This basic model is further modified by incorporating the effects of the existence of a splay fault or local reduction in permeability. The three models and their formulations are described below.

#### 2.2.1. Basic Model

In contrast with R1992, which focused on a vertical strike-slip fault zone, this study attempts to examine the effective normal stress on a subduction plate interface $\sigma_e$. One of the most well-studied subduction zones is the Nankai Trough, where the Philippine Sea Plate subducts beneath southwest Japan. Figure 1a shows an overview of the tectonic setting of the Kumano transect in the Nankai Trough, as interpreted from seismic

**Figure 1.** (a) Tectonic setting of the Kumano transect in the Nankai Trough interpreted from seismic reflection surveys (modified after Moore et al., 2009). (b) Simplified model of a typical subduction zone. Sediments are subducting at pla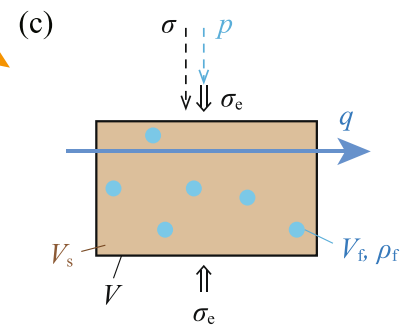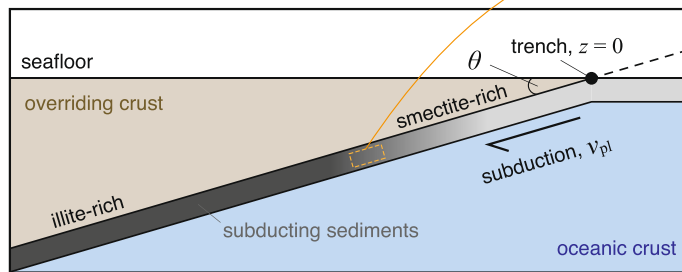te convergence rate $v_{pl}$ and dip angle $\theta$. Note that $\theta$ corresponds to the sum of the angles of both the surface of the accretionary wedge and the subducting sediments. Smectite in sediments transforms into illite with depth owing to dehydration reaction. Although splay faults are disregarded in our basic model, these are considered by modifying the model (see Section 2.2.2). (c) A sketch showing some variables in our models. $\sigma$, compressive stress normal to the subduction channel; $p$, pore-fluid pressure; $\sigma_e$, effective normal stress; $q$, volumetric fluid flux; $V$, volume of bulk rock; $V_s$, volume of solid phase; $V_f$, volume of fluid; and $\rho_f$, fluid density.

reflection surveys and the locations of boreholes drilled by the NanTroSEIZE project of the Integrated Ocean Drilling Program (Moore et al., 2009). The most significant difference from a strike-slip fault zone is the subduction of sediments sandwiched between overriding and oceanic crusts. Figure 1b shows a simplified model that considers this process, where sediments subduct at a plate convergence rate $v_{pl}$ and dip angle $\theta$. Note that $\theta$ corresponds to the sum of the angles of both the surface of the accretionary wedge and subducting sediments. The effect of splay faults will be discussed later (Section 2.2.2). Tsuji et al. (2014) suggested the existence of a high $p$ layer with a thickness of several kilometers above the oceanic crust based on seismic observations in the Kumano transect. This layer can be considered as a fluid channel, such as the fault zone in R1992, and conceivably corresponds to a subducting sedimentary layer. We assume that the subducting sedimentary layer acts as a fluid channel, and the fluid flows only along it. As in R1992, we assumed that the fluid was supplied from the base of the seismogenic zone and flowed upward, while no assumption was made on $p$ at the base (Section 2.4). The fluid input at this seismogenic base may have originated in the serpentinized mantle or dehydration of minerals other than smectite (e.g., Hyndman & Peacock, 2003). For simplicity, we assumed no lateral heterogeneity in the direction of the trench axis and uniform properties across the subduction channel. These assumptions led to a one-dimensional problem in the direction of plate subduction. The $z$-axis is set along the subducting plate interface with $z = 0$ at the trench and positive upward. The model considers the following typical phenomena in subduction zones (Figure 1c): volume changes of rock, solid phase, and fluid due to subduction, changes in fluid properties, fluid generation by smectite dehydration, and advection and diffusion of fluid. In the shallow portion of the subduction zone, the sediments are rich in smectite, which transforms to illite as depth increases owing to the dehydration reaction (Figure 1b). Because the amount of amorphous silica in the sediments in the Kumano transect is approximately 1 wt% (Spinelli & Hutton, 2013), our models do not consider the fluid release caused by the transition from amorphous silica to quartz via opal-CT.

The mass conservation law of fluid in Lagrangian form is expressed as follows:

$$\frac{Dm_f}{Dt} + \frac{\partial(\rho_f qV)}{\partial z} = \omega, \tag{4}$$

where $m_f$ [M] is the fluid mass, $V\left[L^3/L^{-2}\right]$ is the rock volume per unit area of a plane parallel to the subduction channel (sediment thickness), $\omega\left[\text{M T}^{-1}\right]$ is the source of fluid mass caused by smectite dehydration in the basic model, and $m_f = \rho_f V_f$, where $V_f\left[L^3/L^{-2}\right]$ is the fluid volume per unit area of a plane parallel to the subduction channel. Unlike in R1992, we assume that the fluid density is a function of pore-fluid pressure and temperature, which can be expressed as follows:

$$\frac{D\rho_f}{Dt} = \rho_f \beta_f \frac{Dp}{Dt} + \rho_f \lambda_f \frac{DT}{Dt}, \tag{5}$$

where $T$ is the temperature, and for simplicity, we assume a constant geothermal gradient, $T_g$, such that $T = T^0 - T_g z \sin\theta$, where $T^0$ is the temperature at the trench. $\beta_f$ and $\lambda_f$ are the isothermal compressibility and isobaric thermal expansivity of the fluid, respectively. They are assumed to be functions of $p$ and $T$ as in the case of fluid density: $\beta_f = \beta_f(p, T)$, $\lambda_f = \lambda_f(p, T)$. By combining Equations 4 and 5, we obtain

$$(V - V_s)\beta_f \frac{Dp}{Dt} = (V - V_s)\lambda_f \frac{DT}{Dt} - \frac{DV}{Dt} + \frac{DV_s}{Dt} - \frac{1}{\rho_f}\frac{\partial Q_m}{\partial z} + \frac{\omega}{\rho_f}, \tag{6}$$

where $V_s(= V - V_f)$ is the solid volume per unit area of a plane parallel to the subduction channel, and $Q_m = \rho_f qV$ is the mass flux of the fluid. Note that $(-DV/Dt + DV_s/Dt)$ can be interpreted as a source of $p$ owing to porosity change. From Darcy's law, we obtain

$$Q = -\frac{K}{\eta_f}\left(\frac{\partial p}{\partial z} + \rho_f g \sin\theta\right), \tag{7}$$

where $Q = qV$ and $K = kV$. Unlike in R1992, we assume that $\eta_f$ depends on $p$ and $T$ : $\eta_f = \eta_f(p, T)$.

In and around a subduction zone, stress state can become complicated. For instance, van Zelst et al. (2022) showed through two-dimensional numerical modeling of a subduction zone that the direction of maximum principal stress changes from almost horizontal at the shallow portion to almost vertical at the deeper region. This indicates that $\sigma$ is greater than the lithostatic pressure $\rho g(-z)\sin\theta$ at the shallow portion, whereas it becomes smaller at the deeper region. Therefore, it is difficult to uniquely assess the proper relationship between $\sigma$ and lithostatic pressure. To simplify our model, we assume that $\sigma$ is equivalent to the lithostatic pressure at any depth, as in R1992.

The subducting sediments in the Kumano transect mainly consist of mudstone and sandstone (e.g., Expedition 316 Scientists, 2009; Expedition 322 Scientists, 2010). Assuming that each rock unit has a layered structure of the subduction channel and deforms independently, the volume change in Equation 6 can be expressed as follows:

$$\frac{DV}{Dt} = \sum_{(\#)} \frac{DV_{(\#)}}{Dt}, \frac{DV_s}{Dt} = \sum_{(\#)} \frac{DV_{s(\#)}}{Dt}, \tag{8}$$

where subscript (#) indicates the rock type (mudstone or sandstone). Similarly, the source of fluid mass caused by smectite dehydration $\omega_{sm}$ is expressed as follows:

$$\omega_{sm} = \sum_{(\#)} \omega_{sm(\#)}. \tag{9}$$

If we define the volume ratio of mudstone to bulk rock as $\alpha = V_{(mud)}/V$, the permeability of the bulk rock is expressed as follows:

$$k = \alpha k_{(mud)} + (1 - \alpha)k_{(sand)} = \frac{1}{V}\sum_{(\#)} k_{(\#)}V_{(\#)}. \tag{10}$$

We have presented the expression for each variable for each rock type below.

For the Nankai sediments, $k$ is a rapidly decreasing function of effective pressure (e.g., Kitajima & Saffer, 2014; Tanikawa et al., 2014), which clearly represents the effect of mechanical compaction. Under the assumption that effective pressure in their experiments is equivalent to $\sigma_e$ in our formulations, we adopted a simple exponential function of $\sigma_e$ to express the stress dependence of $k$ as in R1992. This exponential function adequately explains the experimental results of certain previous studies and is discussed in detail in Section 2.3.3.

The following four assumptions are made to model the rock volume. First, rocks deform only in the direction normal to the subduction channel. Second, $V$ can be expressed by an equation of state as a function of $\sigma_e$, $T$, and reacted fraction $\xi$, $V = V(\sigma_e, T, \xi)$. Note that the dependence of $V$ on $\sigma_e$, $T$, and $\xi$ represents the effects of mechanical compaction, thermal expansion, and smectite dehydration, respectively. Third, $V$ during the reaction can be expressed as a linear combination of the volumes before and after the reaction, $V(\sigma_e, T, \xi) = (1 - \xi)V(\sigma_e, T, 0) + \xi V(\sigma_e, T, 1)$. Fourth, the isothermal compressibility $\beta$ and isobaric thermal expansivity $\lambda$ of bulk rocks are constant, thereby yielding (Text S1 in Supporting Information S1)

$$\frac{DV}{Dt} = \frac{D\xi}{Dt}\left[V^0(1) - V^0(0)\right]\exp\left[-\beta\left(\sigma_e - \sigma_e^0\right) + \lambda\left(T - T^0\right)\right] + V\left(-\beta\frac{D\sigma_e}{Dt} + \lambda\frac{DT}{Dt}\right), \tag{11}$$

where $V^0(\xi)$ is the rock volume at the trench, and $\sigma_e^0$ is the effective normal stress at the trench. Assuming rigid crystalline grains ($\beta_s = 0$), we obtain a similar expression for the solid-phase volume $V_s$ as follows:

$$\frac{DV_s}{Dt} = \frac{D\xi}{Dt}\left[V_s^0(1) - V_s^0(0)\right]\exp\left[\lambda_s\left(T - T^0\right)\right] + V_s\lambda_s\frac{DT}{Dt}, \tag{12}$$

where $V_s^0(\xi)$ is the volume of the solid phase at the trench, and $\lambda_s$ is the isobaric thermal expansivity of the solid phase.

A chemical formula for smectite dehydration is expressed as follows:

$$\chi_{sm}[\text{smectite}](s) \rightarrow \chi_{il}[\text{illite}](s) + \chi_f H_2O + \chi_{Si}Si^{4+}(aq), \tag{13}$$
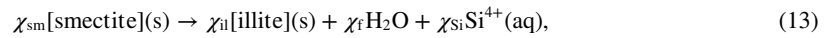
where $\chi_{sm}$, $\chi_{il}$, $\chi_f$, and $\chi_{Si}$ are the molar numbers of smectite, illite, water, and silica, respectively. As shown in Equation 13, for simplicity, our basic model assumes that silica in the product is dissolved in the pore fluid and will flow out of the system; hence, the effect of silica cementation is not considered. This will be considered later as the existence of an impermeable zone, as described in Section 2.2.3. Assuming that the mass change of smectite is only related to this dehydration reaction, we can express the source of fluid mass caused by dehydration $\omega_{sm}$ as follows (Text S2 in Supporting Information S1):

$$\omega_{sm} = \frac{\chi_f M_f}{\chi_{sm} M_{sm}}\rho_{sm}^0 V_{sm}^0(0)\frac{D\xi}{Dt}, \tag{14}$$

where $M_{sm}$ and $M_f$ are the molar masses of smectite and water, respectively; $\rho_{sm}^0$ is the grain density of smectite at the trench, and $V_{sm}^0(\xi)$ is the volume of smectite at the trench.

Based on laboratory experiments, Huang et al. (1993) suggested that the kinetics of the smectite-to-illite transition can be expressed as follows:

$$\frac{DS}{Dt} = -A\left[K^+\right]S^2 \exp\left(-\frac{E}{RT}\right), \tag{15}$$

where $S$ is the mole fraction of smectite in the mixed-layer illite/smectite, $A$ is the frequency factor, $\left[K^+\right]$ is the concentration of potassium, $E$ is the activation energy, and $R$ is the gas constant. Furthermore, from Equations 13 and 15, we obtain

$$\xi = \frac{(1 - S)\chi_{sm}}{(1 - S)\chi_{sm} + S\chi_{il}}, \quad \frac{D\xi}{Dt} = -\frac{\chi_{sm}\chi_{il}}{\left[(1 - S)\chi_{sm} + S\chi_{il}\right]^2}\frac{DS}{Dt}. \tag{16}$$

Although there are different published models (e.g., Pytte & Reynolds, 1989), the selection of reaction kinetics and its parameters should only have minor effects, as discussed in Section 4.5.1. Illite is further transformed into muscovite with the increase in $T$, typically within the range of 200–300°C (e.g., Hunziker, 1986). Because this

reaction does not generate water, the illite-to-muscovite transition can be disregarded in our models under the assumption of no volume change by the reaction.

At a steady state, as in R1992, the terms of the time partial derivative vanish, and only the terms of the spatial derivative remain. In short, we need to solve the following set of ordinary differential equations in terms of $z$:

$$\frac{\mathrm{d}\sigma}{\mathrm{d}z} = -\rho g \sin\theta, \frac{\mathrm{d}p}{\mathrm{d}z} = -\frac{\eta_{\mathrm{f}} Q}{K} - \rho_{\mathrm{f}} g \sin\theta, \frac{\mathrm{d}\sigma_{\mathrm{e}}}{\mathrm{d}z} = \frac{\mathrm{d}\sigma}{\mathrm{d}z} - \frac{\mathrm{d}p}{\mathrm{d}z}, \frac{\mathrm{d}T}{\mathrm{d}z} = -T_{\mathrm{g}} \sin\theta, \tag{17}$$

$$\frac{\mathrm{d}\rho_{\mathrm{f}}}{\mathrm{d}z} = \rho_{\mathrm{f}} \left( \beta_{\mathrm{f}} \frac{\mathrm{d}p}{\mathrm{d}z} - \lambda_{\mathrm{f}} \frac{\mathrm{d}T}{\mathrm{d}z} \right), \frac{\mathrm{d}Q}{\mathrm{d}z} = \frac{1}{\rho_{\mathrm{f}}} \frac{\mathrm{d}Q_{\mathrm{m}}}{\mathrm{d}z} - \frac{Q}{\rho_{\mathrm{f}}} \frac{\mathrm{d}\rho_{\mathrm{f}}}{\mathrm{d}z}, \tag{18}$$

$$\frac{\mathrm{d}Q_{\mathrm{m}}}{\mathrm{d}z} = (V - V_{\mathrm{s}}) v_{\mathrm{pl}} \rho_{\mathrm{f}} \beta_{\mathrm{f}} \frac{\mathrm{d}p}{\mathrm{d}z} - (V - V_{\mathrm{s}}) v_{\mathrm{pl}} \rho_{\mathrm{f}} \lambda_{\mathrm{f}} \frac{\mathrm{d}T}{\mathrm{d}z} + v_{\mathrm{pl}} \rho_{\mathrm{f}} \frac{\mathrm{d}V}{\mathrm{d}z} - v_{\mathrm{pl}} \rho_{\mathrm{f}} \frac{\mathrm{d}V_{\mathrm{s}}}{\mathrm{d}z} + \omega, \tag{19}$$

$$\frac{\mathrm{d}K}{\mathrm{d}z} = \sum_{(\#)} \left[ k_{(\#)} \frac{\mathrm{d}V_{(\#)}}{\mathrm{d}z} + V_{(\#)} \frac{\mathrm{d}k_{(\#)}}{\mathrm{d}z} \right], \frac{\mathrm{d}k_{(\#)}}{\mathrm{d}z} = -\frac{k_{(\#)}}{\sigma_{(\#)}^*} \frac{\mathrm{d}\sigma_{\mathrm{e}}}{\mathrm{d}z}, \tag{20}$$

$$\frac{\mathrm{d}V}{\mathrm{d}z} = \sum_{(\#)} \frac{\mathrm{d}V_{(\#)}}{\mathrm{d}z}, \frac{\mathrm{d}V_{\mathrm{s}}}{\mathrm{d}z} = \sum_{(\#)} \frac{\mathrm{d}V_{\mathrm{s}(\#)}}{\mathrm{d}z}, \tag{21}$$

$$\frac{\mathrm{d}V_{(\#)}}{\mathrm{d}z} = \frac{\mathrm{d}\xi_{(\#)}}{\mathrm{d}z} \left[ V_{(\#)}^0(1) - V_{\mathrm{s}(\#)}^0(0) \right] \exp\left[ -\beta_{(\#)} \left( \sigma_{\mathrm{e}} - \sigma_{\mathrm{e}}^0 \right) + \lambda_{(\#)} \left( T - T^0 \right) \right] + V_{(\#)} \left[ -\beta_{(\#)} \frac{\mathrm{d}\sigma_{\mathrm{e}}}{\mathrm{d}z} + \lambda_{(\#)} \frac{\mathrm{d}T}{\mathrm{d}z} \right], \tag{22}$$

$$\frac{\mathrm{d}V_{\mathrm{s}(\#)}}{\mathrm{d}z} = \frac{\mathrm{d}\xi_{(\#)}}{\mathrm{d}z} \left[ V_{\mathrm{s}(\#)}^0(1) - V_{\mathrm{s}(\#)}^0(0) \right] \exp\left[ \lambda_{\mathrm{s}(\#)} \left( T - T^0 \right) \right] + V_{\mathrm{s}(\#)} \lambda_{\mathrm{s}(\#)} \frac{\mathrm{d}T}{\mathrm{d}z}, \tag{23}$$

$$\omega = \omega_{\mathrm{sm}} = -v_{\mathrm{pl}} \frac{\chi_{\mathrm{f}} M_{\mathrm{f}}}{\chi_{\mathrm{sm}} M_{\mathrm{sm}}} \rho_{\mathrm{sm}}^0 \sum_{(\#)} \left[ V_{\mathrm{sm}(\#)}^0(0) \frac{\mathrm{d}\xi_{(\#)}}{\mathrm{d}z} \right], \tag{24}$$

$$\frac{\mathrm{d}\xi_{(\#)}}{\mathrm{d}z} = -\frac{\chi_{\mathrm{sm}} \chi_{\mathrm{il}}}{\left[ (1 - S_{(\#)}) \chi_{\mathrm{sm}} + S_{(\#)} \chi_{\mathrm{il}} \right]^2} \frac{\mathrm{d}S_{(\#)}}{\mathrm{d}z}, \tag{25}$$

$$\frac{\mathrm{d}S_{(\#)}}{\mathrm{d}z} = -A \left[ \mathrm{K}^+ \right] S_{(\#)}^2 \exp\left( -\frac{E}{RT} \right). \tag{26}$$

These equations are numerically solved by the explicit Runge-Kutta-Fehlberg method of order 5(4) using the open-source Python function scipy.integrate.solve_ivp (SciPy v1.6.2).

### 2.2.2. Model Accounting for Existence of a Splay Fault

Several splay faults branching from the décollement exist in the Kumano transect (Figure 1a), which may be important for understanding the fluid behavior in subduction zones. Lauer and Saffer (2012) performed two-dimensional finite element modeling by incorporating fluid flow along the splay faults in the Costa Rican subduction margin and suggested that they may capture 6%–35% of the total volumetric fluid flux in a steady state. Motivated by this, we examined the effect of fluid leakage from the main subduction channel, which abruptly changes $Q_{\mathrm{m}}$ at the depth of a branching point. This can be modeled by adding a new fluid source term to the conservation of the fluid mass as follows:

$$\omega = \omega_{\mathrm{sm}} + \omega_{\mathrm{sp}}, \tag{27}$$

where $\omega_{\mathrm{sp}}$ is the source of fluid mass caused by a splay fault. To perform numerical integration efficiently, we modeled $\omega_{\mathrm{sp}}$ as a smooth function of $z$ rather than a sum of delta functions for many spray faults as follows:

$$\omega_{\mathrm{sp}} = Q_{\mathrm{m(splay)}} \frac{\mathrm{d}}{\mathrm{d}z} [\mathrm{shvs}(z - z_1)], \tag{28}$$

where $Q_{\mathrm{m(splay)}}$ is the mass flux of the fluid in the splay fault, $z_1$ represents the bottom of the branching area, and $\mathrm{shvs}(z)$ is an infinitely differentiable Heaviside-like function,

$$\text{shvs}(z) = \begin{cases} \frac{1}{2}\left[1 + \tanh\left(\frac{r_1}{z - r_1} + \frac{r_1}{z}\right)\right] & (0 < z < r_1) \\ 0 & (z \geq r_1) \\ 1 & (z \leq 0) \end{cases}, \tag{29}$$

where $r_1$ is the width of the branching area (Figures S1a and S1b in Supporting Information S1). If we define the ratio of $Q_{\text{m(splay)}}$ to $Q_m^0 = \rho_f^0 q^0 V^0$ as $\gamma$, then

$$\omega_{\text{sp}} = \begin{cases} \gamma \rho_f^0 q^0 V^0 \frac{d}{dz}[\text{shvs}(z - z_1)] & (z_1 < z < z_1 + r_1) \\ 0 & (z \leq z_1, z_1 + r_1 \leq z) \end{cases}. \tag{30}$$

After replacing Equation 24 with Equation 27, we numerically solved a series of ordinary differential equations using the same method as in Section 2.2.1.

### 2.2.3. Model Accounting for Local Permeability Reduction

In addition to the mechanical compaction, permeability of the subduction channel may be further influenced by various clogging processes of conduits in rocks. For example, silica is transported in the fluid and precipitates as quartz veins in the rock following silica-water kinetics (e.g., Rimstidt & Barnes, 1980). This process, called silica cementation, has been suggested to control the occurrence of deep slow earthquakes in subduction zones (Audet & Bürgmann, 2014) because it can reduce permeability (e.g., Chester & Logan, 1986). Here, we examined the effect of local reduction in $k$ on $\sigma_e$. The possible mechanisms will be discussed in Section 4.5.4. We express this effect as follows:

$$k_{(\#)} = [1 - \psi\,\text{sbox}(z - z_2)]k_{(\#)}^0 \exp\left(-\frac{\sigma_e}{\sigma_{(\#)}^*}\right), \tag{31}$$

where $\psi$ represents the strength of the clogging effect of conduits, $z_2$ is the peak location of an impermeable zone, and $\text{sbox}(z)$ is an infinitely differentiable boxcar-like function.

$$\text{sbox}(z) = \begin{cases} \frac{1}{2}\left[1 + \tanh\left(\frac{r_2}{|z| - r_2} + \frac{r_2}{|z|}\right)\right] & (|z| < r_2) \\ 0 & (|z| \geq r_2) \end{cases}, \tag{32}$$

where $2r_2$ is the spatial extent of the impermeable zone. It follows from Equation 31 that

$$\frac{dk_{(\#)}}{dz} = -\frac{k_{(\#)}}{\sigma_{(\#)}^*}\frac{d\sigma_e}{dz} - \psi k_{(\#)}^0 \exp\left(-\frac{\sigma_e}{\sigma_{(\#)}^*}\right)\frac{d}{dz}[\text{sbox}(z - z_2)]. \tag{33}$$

The gradient of $\text{sbox}(z)$ at $z = 0$ or $r_2$ is zero. $1 - \psi\,\text{sbox}(z - z_2)$ and its gradients are shown in Figures S1c and S1d in Supporting Information S1, respectively. After replacing Equation 20 with Equation 33, we numerically solve a series of ordinary differential equations using the same method as that used in Section 2.2.1.

### 2.3. Parameter Values Used for Our Models

In this subsection, the parameter values in Equations 17–33 are discussed (Table 1).

#### 2.3.1. Geometrical Constants

We adopted $T_g = 10°C\,\text{km}^{-1}$, approximated from Marcaillou et al. (2012). Because $T$ of the upper limit of the seismogenic zone is approximately 100–150°C (Hyndman et al., 1997), the value of $T_g$ gives an upper limit of seismogenic depth of approximately 10–15 km, which is in good agreement with the lower limit of the source region of shallow slow earthquakes in the Nankai Trough (Nishikawa et al., 2019). The maximum temperature for the brittle behavior of rocks is approximately 350°C (Hyndman et al., 1997). The maximum depth for numerical

**Table 1**
*Values of All the Constants Used in Our Models*

| Parameter | Symbol | Value | Unit | Reference(s) and/or note |
|---|---|---|---|---|
| Geometrical constant | | | | |
| Geothermal gradient | $T_g$ | 10 | $°C\,km^{-1}$ | Marcaillou et al. (2012) |
| Dip angle | $\theta$ | 10 | $°$ | Nakanishi et al. (2002) |
| Seafloor depth of the trench | | 4.35 | km | Figure 1a |
| Plate convergence rate | $v_{pl}$ | 45 | $mm\,yr^{-1}$ | Seno et al. (1993) |
| Thickness of seismogenic crust | $H$ | 35 | km | Hyndman et al. (1997) |
| Bottom of the branching area | $z_1$ | $-45$ | km | Figure 1a |
| Center of the impermeable zone | $z_2$ | $-12.5/\sin(10°)$ | km | |
| Width of the branching area | $r_1$ | 15 | km | Figure 1a |
| Half width of the impermeable zone | $r_2$ | $2.5/\sin(10°)$ | km | |
| Kinetics of smectite dehydration | | | | |
| Mole number of smectite | $\chi_{sm}$ | 1 | mol | Boles and Franks (1979) |
| Mole number of illite | $\chi_{il}$ | 1 | mol | Boles and Franks (1979) |
| Mole number of $H_2O$ | $\chi_f$ | 10 | mol | Boles and Franks (1979) |
| Activation energy | $E$ | 117.152 | $kJ\,mol^{-1}$ | Huang et al. (1993) |
| Frequency factor | $A$ | $8.08 \times 10^4$ | $L\,mol^{-1}\,s^{-1}$ | Huang et al. (1993) |
| Concentration of potassium | $[K^+]$ | $8 \times 10^{-3}$ | $mol\,L^{-1}$ | Expedition 316 Scientists (2009) |
| Gas constant | $R$ | 8.314 | $J\,K^{-1}\,mol^{-1}$ | General value |
| Physical properties | | | | |
| Bulk rock density | $\rho$ | 2700 | $kg\,m^{-3}$ | General value |
| Thermal expansivity of bulk rock | $\lambda$ | $1 \times 10^{-5}$ | $K^{-1}$ | Equivalent to $\lambda_s$ |
| Thermal expansivity of solid phase | $\lambda_s$ | $1 \times 10^{-5}$ | $K^{-1}$ | Schön (2015) |
| Permeability of mudstone at the trench | $k^0_{(mud)}$ | $10^{-16.8}$ | $m^2$ | Tanikawa et al. (2014) |
| Permeability of sandstone at the trench | $k^0_{(sand)}$ | $10^{-14.9}$ | $m^2$ | Kitajima and Saffer (2014) |
| Characteristic stress of mudstone | $\sigma^*_{(mud)}$ | 8.44 | MPa | Tanikawa et al. (2014) |
| Characteristic stress of sandstone | $\sigma^*_{(sand)}$ | 22.0 | MPa | Kitajima and Saffer (2014) |
| Bulk compressibility of mudstone | $\beta_{(mud)}$ | $0.89 \times 10^{-9}$ | $Pa^{-1}$ | Tanikawa et al. (2014) |
| Bulk compressibility of sandstone | $\beta_{(sand)}$ | $2.5 \times 10^{-9}$ | $Pa^{-1}$ | Kitajima and Saffer (2014) |
| Porosity of mudstone at the trench | $\phi^0_{(mud)}$ | 0.338 | | Tanikawa et al. (2014) |
| Porosity of sandstone at the trench | $\phi^0_{(sand)}$ | 0.354 | | Kitajima and Saffer (2014) |
| Viscosity of fluid | $\eta_f$ | $\eta_f(p, T)$ | Pa s | IAPWS95; Wagner and Pruß (2002) |
| Isothermal compressibility of fluid | $\beta_f$ | $\beta_f(p, T)$ | $Pa^{-1}$ | IAPWS95; Wagner and Pruß (2002) |
| Isobaric thermal expansivity of fluid | $\lambda_f$ | $\lambda_f(p, T)$ | $K^{-1}$ | IAPWS95; Wagner and Pruß (2002) |
| Mineralogical properties | | | | |
| Molar mass of quartz | | 60.09 | $g\,mol^{-1}$ | General value |
| Molar mass of plagioclase | | 262.24 | $g\,mol^{-1}$ | General value |
| Molar mass of smectite | $M_{sm}$ | 4028.35 | $g\,mol^{-1}$ | Boles and Franks (1979) |
| Molar mass of illite | $M_{il}$ | 3864.315 | $g\,mol^{-1}$ | Boles and Franks (1979) |
| Molar mass of kaolinite | | 258.172 | $g\,mol^{-1}$ | General value |
| Molar mass of chlorite | | 281.7904 | $g\,mol^{-1}$ | Kameda et al. (2011) |
| Grain density of quartz at the trench | | 2648 | $kg\,m^{-3}$ | Schön (2015) |

**Table 1**
*Continued*

| Parameter | Symbol | Value | Unit | Reference(s) and/or note |
|---|---|---|---|---|
| Grain density of plagioclase at the trench | | 2620 | $kg\,m^{-3}$ | Schön (2015) |
| Grain density of smectite at the trench | $\rho_{sm}^0$ | 2332 | $kg\,m^{-3}$ | Boles and Franks (1979); Bird (1984); Schön (2015) |
| Grain density of illite at the trench | | 2660 | $kg\,m^{-3}$ | Schön (2015) |
| Grain density of kaolinite at the trench | | 2594 | $kg\,m^{-3}$ | Schön (2015) |
| Grain density of chlorite at the trench | | 2800 | $kg\,m^{-3}$ | Schön (2015) |

integration (thickness of seismogenic crust) is, thus, set to $H = 35\,km$ because at temperatures exceeding 350°C, deformation of rocks is dominated by plastic flow rather than cataclasis, and the stress dependences assumed for rock volume and permeability may not be applicable. The depth of the trench from the sea surface is 4.35 km (Figure 1a), and the sediments subduct from the trench at a plate convergence rate, $v_{pl}$, of 45 mm yr$^{-1}$ (Seno et al., 1993) and a dip angle, $\theta$, of 10° (sum of the angles of the surface of the accretionary wedge 3° and the subducting oceanic crust 7°; Nakanishi et al., 2002). In the model with a splay fault, the bottom and width of the branching area are roughly estimated from Figure 1a as $z_1 = -45\,km$ and $r_1 = 15\,km$, respectively. When incorporating the local reduction in $k$, we need to determine the location of the impermeable zone $z_2$ and its spatial extent $2r_2$, both of which are dependent on the mechanisms that generate the impermeable zone. If we assume that permeability decreases owing to silica cementation driven by release of silica from smectite dehydration (see Section 4.5.4 for the detailed discussion), one potential clue can be obtained by referring to the values of smectite dehydration. Although the peak depth of the dehydration reaction differs slightly between mudstone and sandstone (Figure S2 in Supporting Information S1), we consider a depth of 12.5 km as a representative peak location of smectite dehydration, whose depth extent is estimated to be approximately 5 km. We assume that the location of the impermeable zone and its depth extent are 12.5 and 5 km, corresponding to $z_2 = -12.5/\sin(10°)\,km$ and $r_2 = 2.5/\sin(10°)\,km$, respectively. As reference, we also performed calculations for the various $z_2$ values.

### 2.3.2. Parameters Regarding Dehydration Reaction of Smectite

The constants in the chemical formula for smectite dehydration were adopted from the study of Boles and Franks (1979) as $\chi_{sm} = \chi_{il} = 1$ and $\chi_f = 10$. The kinetic parameters for dehydration were obtained from the studies of Huang et al. (1993) and Expedition 316 Scientists (2009) as follows: activation energy $E = 117.152\,kJ\,mol^{-1}$, frequency factor $A = 8.08 \times 10^4\,L\,mol^{-1}\,s^{-1}$, concentration of potassium $[K^+] = 8 \times 10^{-3}\,mol\,L^{-1}$, and gas constant $R = 8.314\,J\,K^{-1}\,mol^{-1}$. Although $[K^+]$ can vary with depth, owing to the lack of information, its value is assumed to be constant and equal to the measured concentration in pore fluids near the décollement.

### 2.3.3. Physical Properties

As a typical value, the bulk rock density was assumed to be $\rho = 2700\,kg\,m^{-3}$. The thermal expansivity of the pores is equal to $\lambda_s$, so $\lambda = \lambda_s$. We adopted $\lambda_s = 1 \times 10^{-5}\,K^{-1}$, which was reported by Schön (2015) as that of quartz grains. The physical properties related to permeability and porosity were determined from the experimental data of Tanikawa et al. (2014) and Kitajima and Saffer (2014), who performed consolidation and permeability tests using mudstone and sandstone core samples collected from the Nankai Trough during the NanTroSEIZE project, respectively. As typical samples of mudstone and sandstone in the Nankai sediments, we refer to the experimental results obtained using mudstone collected from 402.48 mbsf in Site C0007D (C7D-4 in Tanikawa et al., 2014) and sandstone collected from 781 mbsf in Site C0011B (U211 in Kitajima & Saffer, 2014), respectively. By performing least-squares fitting on the reported data (Figure S3 in Supporting Information S1), we determined $k^0_{(mud)} = 10^{-16.8}\,m^2$, $k^0_{(sand)} = 10^{-14.9}\,m^2$, $\sigma^*_{(mud)} = 8.44\,MPa$, $\sigma^*_{(sand)} = 22.0\,MPa$, $\beta_{(mud)} = 0.89 \times 10^{-9}\,Pa^{-1}$, $\beta_{(sand)} = 2.5 \times 10^{-9}\,Pa^{-1}$, $\phi^0_{(mud)} = 0.338$, and $\phi^0_{(sand)} = 0.354$ (Text S3 in Supporting Information S1). The viscosity, thermal expansivity, and compressibility of fluid are rather involved functions of $p$ and $T$ (Wagner & Pruß, 2002). We used the open-source Python function iapws.iapws95.IAPWS95 (iapws v1.5.2) to calculate these fluid properties based on a formulation developed by the International Association for the Properties of Water and Steam in 1995 and modified in 2016 (see Wagner & Pruß, 2002 for the detailed formulation).

### 2.3.4. Mineralogical Properties

The representative mineral compositions of mudstone were roughly estimated from Expedition 316 Scientists (2009) and Guo and Underwood (2012) as 20 wt% quartz, 15 wt% plagioclase, 25 wt% smectite, 25 wt% illite, 5 wt% kaolinite, and 10 wt% chlorite. Similarly, the mineral composition representing the Nankai sandstone was estimated from Expedition 322 Scientists (2010) and Underwood & Guo (2013) to be 30 wt% quartz, 40 wt% plagioclase, and 30 wt% smectite. Molar mass of each mineral phase was calculated from the general chemical formula, Boles and Franks (1979), and Kameda et al. (2011) as follows: quartz, 60.09 g mol$^{-1}$; plagioclase, 262.24 g mol$^{-1}$; smectite, 4,028.35 g mol$^{-1}$; illite, 3,864.315 g mol$^{-1}$; kaolinite, 258.172 g mol$^{-1}$; and chlorite, 281.7904 g mol$^{-1}$. The grain densities at the trench of each mineral, except smectite, were set from Schön (2015) as follows: quartz, 2,648 kg m$^{-3}$; plagioclase, 2,620 kg m$^{-3}$; illite, 2,660 kg m$^{-3}$; kaolinite, 2,594 kg m$^{-3}$; and chlorite, 2,800 kg m$^{-3}$. In the chemical equation presented by Boles and Franks (1979), 2 mol of interlayer water per unit cell of $O_{20}(OH)_4$ are present in smectite particles, which corresponds to 1.25 nm $d$-spacing (Bird, 1984). Because the $d$-spacing value of smectite without the interlayer water is 1 nm (Bird, 1984), the thickness of the interlayer water is 0.25 nm. Assuming that the grain density of smectite without interlayer water is the same as that of illite, $\rho_{sm}^0 = 2332 \, \text{kg m}^{-3}$.

### 2.4. Boundary Conditions at the Trench

In general, a unique solution for a system of ordinary differential equations can be obtained if the values of the variables are given at a certain point (i.e., boundary condition). Here, we focus on the trench ($z = 0$) as the boundary because most of the variables there can be calculated from the results of the NanTroSEIZE project and subsequent analysis of the collected core samples. Therefore, as in R1992, our calculations were performed without any assumption on the values of all variables at any depth other than the trench. Among the variables of the basic model, we conducted a parameter study in terms of the volumetric fluid flux at the trench $q^0$, which is probably the most poorly constrained parameter because of scarcity of observations. In addition, we examined the effect of the volume fraction of mudstone at trench $\alpha^0$. Given the values of $q^0$ and $\alpha^0$, a unique solution for Equations 17–26 can be obtained as a solution to the system of ordinary differential equations. To illuminate the effects of fluid leakage through the splay fault and local reduction in $k$, we select a typical case in the basic model and perform additional parameter studies on it in terms of $\gamma$ and $\psi$. The basic model corresponds to $\gamma = \psi = 0$.

The other variables at the trench can be determined from the various constants mentioned in Section 2.3. Because the trench is located at 4.35 km below the sea surface, $\sigma^0$ and $p^0$ are roughly estimated to be 43.5 MPa where $\sigma_e^0 = 0$. The temperature at the trench in the Kumano transect was measured by Expedition 316 Scientists (2009) as $T^0 = 1.6°C$. The fluid density was calculated from $p^0$ and $T^0$ using the IAPWS95 module as $\rho_f^0 = 1021 \, \text{kg m}^{-3}$. The mole fraction of smectite in the mixed-layer illite/smectite can be calculated from the molar mass and the mineral composition of each rock type as $S_{(\text{mud})}^0 = 0.488$ and $S_{(\text{sand})}^0 = 1$, and it follows from Equation 16 that $\xi_{(\text{mud})}^0 = 0.512$ and $\xi_{(\text{sand})}^0 = 0$. The rock volume can take an arbitrary positive value and is thus set to $V^0 = 1 \, \text{m}^3/\text{m}^2$. The permeability depends on $\alpha^0$ and can be expressed using Equation 10 as $k^0 = \alpha^0 k_{(\text{mud})}^0 + (1 - \alpha^0) k_{(\text{sand})}^0$. The values of $Q^0$, $K^0$, and $Q_m^0$ can be calculated from the values of $q^0$, $k^0$, $\rho_f^0$, and $V^0$. The volumes of mudstone and sandstone with reacted fractions $\xi_{(\text{mud})}^0$ and $\xi_{(\text{sand})}^0$ are $V_{(\text{mud})}^0 = \alpha^0 V^0$ and $V_{(\text{sand})}^0 = (1 - \alpha^0) V^0$, respectively, and the corresponding volumes of the solid phase are $V_{s(\#)}^0 = (1 - \phi_{(\#)}^0) V_{(\#)}^0$. The solid phase volumes at any given $\xi$, $V_{s(\#)}^0(\xi)$, can be calculated from the mineral composition, molar mass, chemical formula, and grain density. Because the effect of smectite dehydration on the porosity is unknown, we assume that $\phi$ of the sediments is independent of $\xi$ at $\sigma_e = \sigma_e^0$ and $T = T^0$. Therefore, the bulk rock volumes at any given $\xi$ can be calculated as $V_{s(\#)}^0(\xi)/(1 - \phi_{(\#)}^0)$. Certain variables at the trench and other unknown parameters are listed in Table 2.

It should be noted here that a positive source of $p$ decreases $p$ below it, as discussed in the following section. Although apparently counterintuitive, this is owing to our method of giving the boundary condition. To qualitatively clarify this point, we shall consider a simple diffusion equation with a source term $\omega' \, [\text{ML}^{-3} \, \text{T}^{-2}]$ at a steady-state: $d^2p/dz^2 + \omega' = 0$. If $p$ and $q$ are given at $z = 0$, positive $\omega'$ results in negative $d^2p/dz^2$ and positive $dq/dz$, which decreases $p$ and $q$ at a greater depth (largely negative $z$). Additionally, it follows from this simple diffusion equation that a larger $\omega'$ leads to a larger $dq/dz$ around the source and thus a smaller $q$ below it. In our model, both the mechanical effect of subduction and the effect of smectite dehydration can be a positive source term of $p$. The former is associated with increments in $\sigma$ and $T$ in the Lagrangian

**Table 2**
*Boundary Conditions at the Trench and Other Unknown Parameters*

| Parameter | Symbol | Value | Unit[a] | Reference(s) and/or note |
|---|---|---|---|---|
| **Unknown parameter** | | | | |
| Volumetric fraction of mudstone | $\alpha^0$ | | | $0 \leq \alpha^0 \leq 1$ |
| Volumetric fluid flux | $q^0$ | | L T$^{-1}$ | $q^0 > 0$ |
| Strength of the effect of a splay fault | $\gamma$ | | | $\gamma \geq 0$ |
| Strength of the effect of the impermeable zone on $k$ | $\psi$ | | | $0 \leq \psi \leq 1$ |
| **Known parameter** | | | | |
| Compressive stress normal to the subduction channel | $\sigma^0$ | 43.5 | MPa | Moore et al. (2009) |
| Pore-fluid pressure | $p^0$ | 43.5 | MPa | Moore et al. (2009) |
| Effective normal stress | $\sigma_e^0$ | 0 | MPa | $\sigma_e^0 = \sigma^0 - p^0$ |
| Temperature | $T^0$ | 1.6 | °C | Expedition 316 Scientists (2009) |
| Fluid density | $\rho_f^0$ | 1021 | kg m$^{-3}$ | IAPWS95; Wagner and Pruß (2002) |
| Mole fraction of smectite in the I/S mixed layer in mudstone | $S_{(mud)}^0$ | 0.488 | | Expedition 316 Scientists et al. (2009) |
| | | | | Guo and Underwood (2012) |
| Mole fraction of smectite in the I/S mixed layer in sandstone | $S_{(sand)}^0$ | 1 | | Expedition 322 Scientists (2009) |
| | | | | Underwood and Guo (2013) |
| Reacted fraction in mudstone | $\xi_{(mud)}^0$ | 0.512 | | $1 - S_{(mud)}^0$ |
| Reacted fraction in sandstone | $\xi_{(sand)}^0$ | 0 | | $1 - S_{(sand)}^0$ |
| Bulk rock volume per unit area | $V^0$ | 1 | m$^3$ m$^{-2}$ | Arbitrary value |
| Permeability of mudstone | $k_{(mud)}^0$ | $10^{-16.8}$ | m$^2$ | Tanikawa et al. (2014) |
| Permeability of sandstone | $k_{(sand)}^0$ | $10^{-14.9}$ | m$^2$ | Kitajima and Saffer (2014) |

[a]For $q^0$, dimension is given instead of unit.

description, which squeezes fluids out of the sediments by mechanical compaction and thermally pressurizes them, respectively. Although the latter is always the source of fluid mass, it becomes a negative source term of $p$ in some cases (Section 3.1).

## 3. Results

### 3.1. Basic Model

By performing a numerical integration of Equations 17–26 with different combinations of $q^0$ and $\alpha^0$, we investigated how the $\sigma_e$ distributions change depending on these two parameters. We compared $\sigma_e$ for the three cases of no subduction ($v_{pl} = 0$, constant $\xi$), no reaction (constant $\xi$), and the basic model. Note that the difference in the solution of the no-subduction case from that of R1992 is attributed to the variable fluid properties when $\alpha^0 = 0$ or 1. The $\sigma_e$ distributions obtained can be classified into three types: numerical integration is completed and $\sigma_e$ is always positive (physically sound solution; Figure 2a), numerical integration is completed, but there is a region of negative $\sigma_e$ (negative solution; Figure S4a in Supporting Information S1), and numerical integration diverges and fails to reach the seismogenic base at a depth of 35 km (diverging solution; Figure S4b in Supporting Information S1). When $q^0$ and $\alpha^0$ satisfy the following relationship (Text S4 in Supporting Information S1):

$$\alpha^0 > \frac{(q^0 \eta_f^0) / \left[ (\rho - \rho_f^0) g \sin \theta \right] - k_{(sand)}^0}{k_{(mud)}^0 - k_{(sand)}^0}, \tag{34}$$

$\sigma_e$ just below the trench becomes negative, and a negative solution is obtained. This equation determines the upper bound of $q^0$ for a physically sound solution at a given $\alpha^0$. If $q^0$ is too small, $Q_m$ becomes negative at a certain depth, so $q$ becomes negative, and $\sigma_e$ diverges at a deeper portion (Figure S4b in Supporting Information S1). For the no-subduction case, there is no diverging solution because $Q_m$ does not change with depth, and, in an extreme
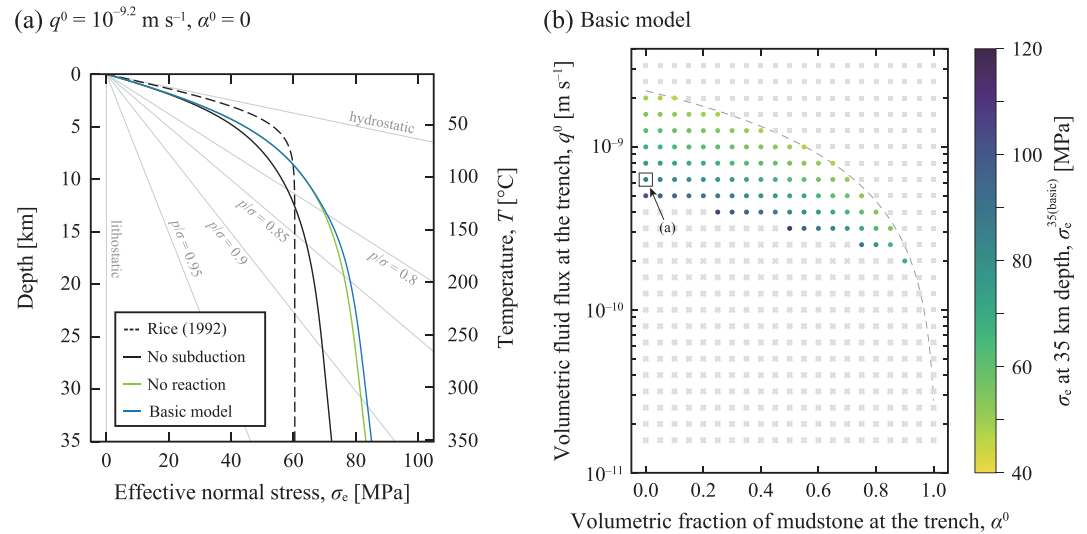
**Figure 2.** (a) Solutions of the basic model obtained by numerically integrating Equations 17–26 with $q^0 = 10^{-9.2}$ m s$^{-1}$ and $\alpha^0 = 0$ for the cases of no subduction (black line), no reaction (green line), and the basic model (blue line). Rice's (1992) solution for an oblique channel is also shown for comparison (dashed black line). Gray lines indicate a depth dependence of $\sigma_e$ at constant values of the pore pressure ratio $p/\sigma$. (b) $\sigma_e$ at the seismogenic base (35 km depth) for the basic model evaluated for various combinations of $q^0$ and $\alpha^0$. Gray squares and crosses indicate that the solutions include negative $\sigma_e$ and never attain a depth of 35 km, respectively. Dashed gray lines are the boundary above which $\sigma_e$ just below the trench takes a negative value (Equation 27).

case, $p$ becomes hydrostatic when $q^0$ is zero. The physically sound solution is obtained only when $q^0$ is between that of the negative and diverging solutions.

Figure 2a shows representative physically sound solutions with $q^0 = 10^{-9.2}$ m s$^{-1}$ and $\alpha^0 = 0$. For comparison, the solution of R1992 was also calculated using Equation 3 by replacing $g$ with $g \sin \theta$. The R1992's solution is based on constant $\rho_f$ and $\eta_f$, and in Figure 2a, both properties were set as the mean values of those obtained for the no-subduction case (Figure S5 in Supporting Information S1). The R1992's solution reaches an asymptotic value of $\sigma_e \simeq 60$ MPa at a depth of approximately 10 km. The solutions for the other three cases all show a similar shape, with a decreasing gradient of $\sigma_e$ at increasing depth. However, in contrast with the R1992's solution, the $\sigma_e$ values of these solutions do not have clear asymptotic values. This comparison indicates that even in the case of a strike-slip fault, the asymptotic $\sigma_e$ at depth in R1992's solution is not obtained when realistic fluid properties are considered. The pore pressure ratio at a depth of 35 km is typically within the range of 0.9–0.95 unless the $q^0$ value is very close to the critical value below which the solution diverges.

We focus on $\sigma_e$ at the seismogenic base (depth of 35 km) as a typical effective normal stress in the seismogenic zone. Figure 2b shows $\sigma_e$ at this depth for the solutions of the basic model, $\sigma_e^{35(basic)}$, calculated in our parameter study as a color contour. The negative and diverging solutions are represented by gray squares and crosses, respectively. At a given $\alpha^0$, $\sigma_e^{35(basic)}$ of physically sound solutions increases with decreasing $q^0$. $\sigma_e^{35(basic)}$ is within the range of 40–120 MPa and typically in the order of tens of MPas, except for the cases with $q^0$ near the critical value.

Figure 3 shows the difference in $\sigma_e$ at a depth of 35 km between the cases with no subduction $\sigma_e^{35(nos)}$ and no reaction $\sigma_e^{35(nor)}$ (Figure 3a), and between the case with no reaction $\sigma_e^{35(nor)}$ and the basic model $\sigma_e^{35(basic)}$ (Figure 3b). The mechanical effect of subduction, $\sigma_e^{35(nor)} - \sigma_e^{35(nos)}$, always takes a positive value (Figure 3a) and, thus, is a source of $p$. By contrast, the effect of smectite dehydration, $\sigma_e^{35(basic)} - \sigma_e^{35(nor)}$, can take either positive or negative values depending on the combination of $q^0$ and $\alpha^0$ (Figure 3b; negative effect is indicated by black-edged circles). Both the $\sigma_e^{35(nor)} - \sigma_e^{35(nos)}$ and $\sigma_e^{35(basic)} - \sigma_e^{35(nor)}$ values diverge at small $q^0$, and numerical integration fails to reach a depth of 35 km even at a smaller $q^0$ (graphs inserted at the lower left of each diagram in Figure 3).

The possibility of smectite dehydration being a sink of $p$ may be counter-intuitive. Whether dehydration becomes a source or a sink of $p$ is determined by the balance of the amount of water released and the change in the fluid
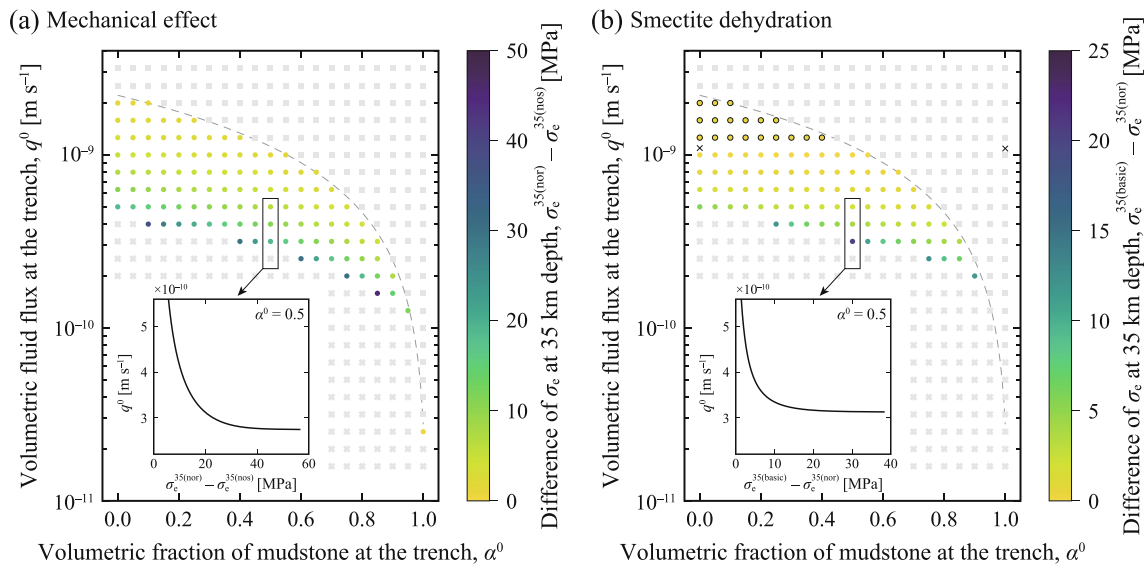
**Figure 3.** Calculation results of the basic model showing the (a) mechanical effect and (b) effect of smectite dehydration on $\sigma_e$ at the seismogenic base (a depth of 35 km) evaluated for various combinations of $q^0$ and $\alpha^0$. The gray squares and crosses and the gray dashed line are the same as those in Figure 2b. Black crosses in (b) indicate the critical $q^0$ value for $\alpha^0 = 0$ or 1 (Equation 28), above which the effect of smectite dehydration becomes a sink of $p$ (indicated by black edged circles). The graphs inserted at the lower left of each figure show the (a) mechanical effect, and (b) effect of smectite dehydration at the seismogenic base around the $q^0$ value that diverges the solution.

volume. The critical condition can be derived from the mass conservation of fluid as follows (Text S5 in Supporting Information S1):

$$q^0 = v_{pl} \left[ \phi^0 + \frac{\chi_f M_f}{\chi_{sm} M_{sm}} \frac{\rho_{sm}^0}{\rho_f^0} \frac{V_{sm}^0(0)}{V^0(0) - V^0(1)} \right], \tag{35}$$

strictly for end-member cases ($\alpha^0 = 0$ or 1). This criterion is indicated by black crosses in Figure 3b, which define the boundary between the positive and negative $\sigma_e^{35(basic)} - \sigma_e^{35(nor)}$ values.

### 3.2. Model Accounting for a Splay Fault

For the model that considers a splay fault, we performed numerical integration of the same equations of the basic model with $q^0 = 10^{-9.2}$ m s$^{-1}$ and $\alpha^0 = 0$; however, Equation 24 is replaced by Equation 27. Figure 4a shows how the $\sigma_e$ distributions change depending on $\gamma$, the strength of the effect of the splay fault. Note that the solution with $\gamma = 0$ is identical to the solution for the basic model. When $\gamma$ is positive, $Q_m$ below the branching area increases, resulting in a decrease in $\sigma_e$ at greater depths relative to the basic model. $\sigma_e$ increases at depths below the branching area owing to the variable fluid properties, similar to that in the basic model. As $\gamma$ increases, $Q_{m(splay)}$ increases linearly, and the quantitative effect of a splay fault on $\sigma_e$ increases. When $\gamma = 20$, $\sigma_e$ becomes negative below the branching area. A physically sound solution requires a smaller value of $q^0$ for such a large $\gamma$.

### 3.3. Model Accounting for Local Permeability Reduction

Similar to the description in the previous section, we selected the solution for the basic model with $q^0 = 10^{-9.2}$ m s$^{-1}$ and $\alpha^0 = 0$ and added the effect of local reduction in $k$ using Equation 33 for Equation 20. Figure 4b shows $\sigma_e$ distributions with different values of $\psi$, the strength factor of the impermeable zone. The solution with $\psi = 0$ was identical to that of the basic model. When $\psi$ is positive, the local decrease in $k$ in the impermeable zone results in a local decrease in $\sigma_e$ there unlike in the case of a splay fault. $\sigma_e$ at a depth sufficiently below the zone converges to that of the basic model. The extremely strong reduction in $k$, namely $\psi = 0.97$, results in a negative $\sigma_e$ in this combination of $q^0$ and $\alpha^0$. We also confirmed that the locally low $\sigma_e$ around the impermeable zone was realized regardless of its location (Figure S6 in Supporting Information S1).
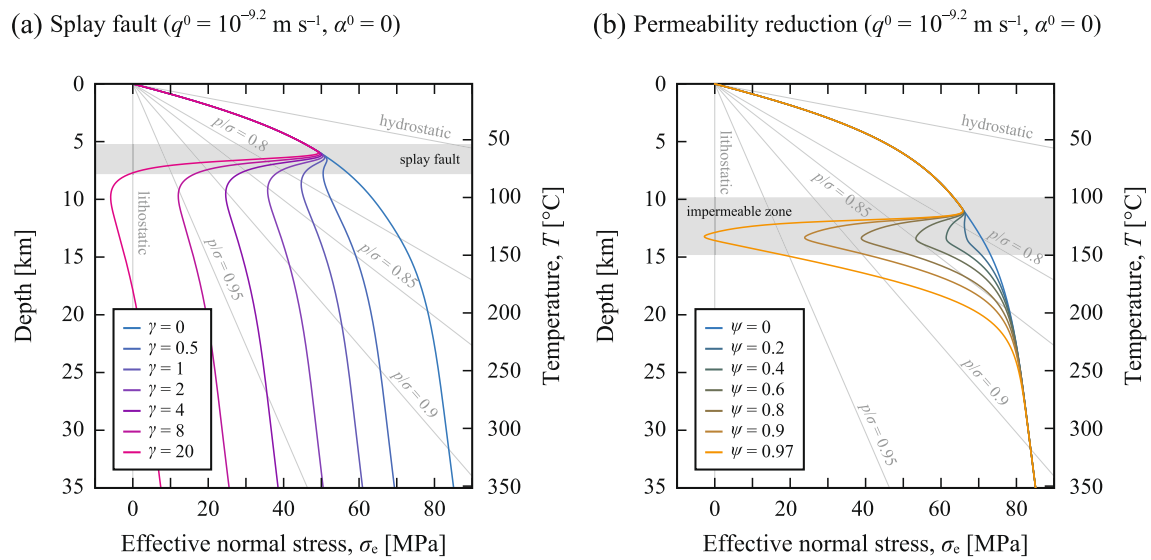
**Figure 4.** Solutions of the models that additionally incorporate the effects owing to (a) the existence of a splay fault and (b) local permeability reduction. We performed numerical integration of the same ordinary differential equations for the basic model with $q^0 = 10^{-9.5}$ m s$^{-1}$ and $\alpha^0 = 0.5$, except that (a) Equation 24 is replaced with Equation 27 and (b) Equation 20 is replaced with Equation 33.

## 4. Discussion

### 4.1. Comparison With Observations at Subduction Zones

Previous studies on subduction zones have suggested the existence of excess pore pressure by seismological observations (Tsuji et al., 2014) and via measurement of the flow rate of fluid out of a borehole (Hirose et al., 2021). These results are consistent with the results of our modeling, where $p$ constantly exceeds hydrostatic pressure (Figures 2a and 4), except at the trench, in physically sound solutions.

In subduction zones worldwide, the stress drop of earthquakes typically ranges from 1 to 10 MPa, with a median value of approximately 3 MPa (Allmann & Shearer, 2009). This range corresponds to $\sigma_e$ in the order of tens of MPas with self-similarity of dynamic growth of a mode II crack (Broberg, 1978) and typical rate dependency (Blanpied et al., 1991) of a laboratory-derived friction law (Dieterich, 1979; Ruina, 1983) (Text S6 in Supporting Information S1). Therefore, the basic model and the model with local permeability reduction yielded results that were consistent with the stress drop estimated from seismological observations. Additionally, our models suggest the depth dependence of $\sigma_e$ in the seismogenic zone because of the implementation of realistic fluid properties. The gradient of $\sigma_e$ is significantly smaller than that expected from hydrostatic $p$ (Figures 2a and 4). However, because of significant scatter in the data of stress drop, typically by a factor of 10 or more, it may be difficult to determine whether this small gradient in $\sigma_e$ is realistic (Figure S7 in Supporting Information S1).

Our results can be considered to be a prediction of the possible range of $q^0$ (Figures 2b and 3). Although continuous measurements of fluid flux in subduction zones have been rare, Solomon et al. (2009) provided a long-term record of the volumetric fluid flux near the trench at the Costa Rican subduction margin. The observed flow rates range from 0.02 to 5 cm yr$^{-1}$, corresponding to $q^0$ of $6.34 \times 10^{-12}$–$1.59 \times 10^{-9}$ m s$^{-1}$, which is consistent with the range of $q^0$ where the physically sound solutions exist in our basic model.

### 4.2. Comparison With Previous Hydraulic Modeling Other Than Rice (**1992**)

This subsection compares the results of some previous hydraulic modeling in subduction zones with those of our calculations. Previous studies have focused on fluid behavior in a two-dimensional system (e.g., Bekins et al., 1995; Ellis et al., 2015; Fulton et al., 2009; Lauer & Saffer, 2012, 2015; Saffer & Bekins, 1998; Spinelli et al., 2006), whereas our calculations are based on one-dimensional modeling. This issue will be discussed in Section 4.5.2.

Previous hydraulic modeling has demonstrated that the pore pressure ratio along a subduction interface increases at a shallow portion and then decreases at a deeper region (e.g., Bekins et al., 1995; Lauer & Saffer, 2015;

Saffer & Bekins, 1998; Spinelli et al., 2006). Such a characteristic is usually absent in the solutions of our basic model, where the pore pressure ratio increases monotonically with depth (Figure 2a). However, when $q^0$ is close to the critical value below which the solution diverges, the pore pressure ratio increases and then decreases with the increase in depth (Figure S8 in Supporting Information S1). When accounting for a splay fault or an impermeable zone, the pore pressure ratio showed increase and subsequent decrease with depth when their effects on $\sigma_e$ are significant (Figure 4). Van Dinther et al. (2013) suggested through earthquake cycle simulations that regular earthquakes in subduction zones can occur only when the pore pressure ratio is within the range from approximately 0.7 to 0.99, which is in agreement with the results of most of our calculations.

Some previous modeling (e.g., Bekins et al., 1995; Saffer & Bekins, 1998) suggested that smectite dehydration was a weaker source of $p$ than mechanical compaction. This argument agrees with the results of our calculations (Figure 3), where the mechanical effect, including compaction, is a stronger source of $p$ than smectite dehydration unless $q^0$ is close to the critical value.

Noteworthy developments of our models from the previous hydraulic modeling include (a) formulations of hydraulic properties based on the experimental results, (b) implementation of the dependence of the fluid properties on $p$, and (c) an attempt to generate locally low $\sigma_e$. Regarding the first, certain previous studies (e.g., Bethke, 1986; Lauer & Saffer, 2012, 2015; Spinelli et al., 2006) expressed porosity as a simple exponential function of depth (Athy's law; Athy, 1930). Permeability has been calculated as a function of porosity (e.g., Bekins et al., 1995; Lauer & Saffer, 2015; Saffer & Bekins, 1998; Spinelli et al., 2006) or rather considered to be constant within one lithological unit (e.g., Lauer & Saffer, 2012). Therefore, the dependences of $\phi$ and $k$ of rocks on $\sigma_e$, which has been examined in laboratory hydraulic experiments (e.g., Ikari & Saffer, 2012; Kitajima & Saffer, 2014; Tanikawa et al., 2012, 2014), are not adequately formulated in these previous modeling. Conversely, we referred to the results of laboratory hydraulic experiments performed by Tanikawa et al. (2014) and Kitajima and Saffer (2014), and therefore, our formulations for these hydraulic properties are more realistic from a perspective of material science. Regarding the second, some previous modeling (e.g., Bekins et al., 1995; Lauer & Saffer, 2012, 2015; Saffer & Bekins, 1998; Spinelli et al., 2006) employed a calculation code called SUTRA developed by Voss (1984). In formulations of SUTRA, density and viscosity of fluid are expressed as a function only of $T$, whereas our models consider their dependence on both $p$ and $T$ (e.g., Equation 5). Regarding the third, the existence of an impermeable zone in subduction zones was already modeled by Fulton et al. (2009). However, their calculations are focused on transient fluid behavior and do not investigate the occurrence of locally low $\sigma_e$ at a certain depth. To our knowledge, the present study is the first to examine the mechanisms responsible for a local decrease in $\sigma_e$ based on hydraulic modeling that considers a local reduction in $k$.

### 4.3. Implication for Earthquake Cycle Simulations

The $\sigma_e$ distribution is an important input boundary condition in modeling the transient fault motion by earthquake cycle simulations. There are two end-member hypotheses: linearly increasing $\sigma_e$ with increasing depth or the existence of an upper bound of $\sigma_e$ based on the R1992's model. Our basic model considers the effect of smectite dehydration, as well as the mechanical effect attributed to plate subduction and the fluid properties that vary with $p$ and $T$; therefore, the calculated $\sigma_e$ distribution can provide a more realistic boundary condition. However, the obtained results are usually close to the R1992's solution in that the gradient of $\sigma_e$ decreases with increasing depth (Figure 2a), and its consequence may not be significantly different from those of models based on R1992 (e.g., Lapusta et al., 2000; Liu & Rice, 2005). If additional effects owing to the existence of a splay fault or local reduction in $k$ are significant, $\sigma_e$ decreases considerably (Figure 4), which may impact the resulting behaviors of fault motion during seismic cycles, as demonstrated by Liu and Rice (2007, 2009).

In this study, we examined solutions with fixed geometrical constants (i.e., $v_{pl}$, $\theta$, and $T_g$), but these parameters vary for different subduction zones (e.g., Saffer & Wallace, 2015) and different regions, even within the same subduction zone (e.g., Seno et al., 1993). Therefore, when performing earthquake cycle simulations in subduction zones, employing typical geometrical constants that are representative of the region of interest in that subduction zone may be crucial. Qualitatively, the larger the value of $T_g$ and the smaller the values of $v_{pl}$ and $\theta$, the more intensive the smectite dehydration at shallower depths and the greater the effect of this reaction on the local $\sigma_e$ around the regions where the reaction occur.
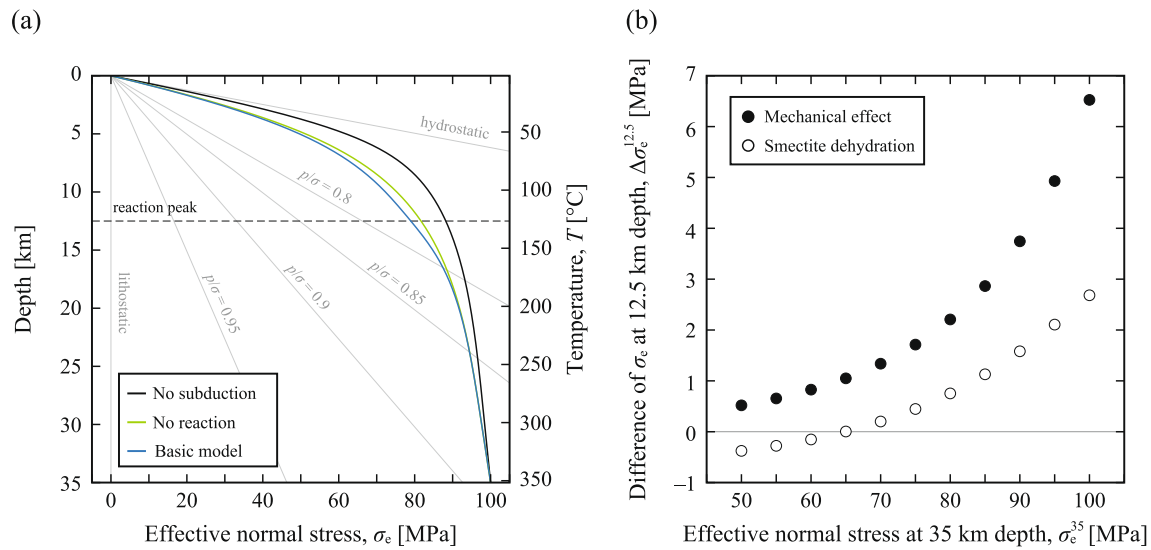
**Figure 5.** (a) Solutions of the basic model obtained by numerically integrating Equations 17–26 with the $\sigma_e$ value at a depth of 35 km being fixed at 100 MPa for the cases of no subduction (black line), no reaction (green line), and the basic model (blue line). Note that the $q^0$ values of all solutions differ from each other. (b) Difference of the $\sigma_e$ values at a depth of 12.5 km owing to the mechanical effect of subduction (black circle) and the effect of smectite dehydration (white circle) as a function of $\sigma_e^{35}$.

### 4.4. Implication for Shallow Slow Earthquakes

For discussing the quantitative effect of smectite dehydration and the mechanical effect of subduction on $\sigma_e$ around the source region of shallow slow earthquakes, comparisons of solutions with constant $\sigma_e^{35}$ can be more informative rather than those with constant $q^0$ as in Figure 3. Therefore, we performed additional calculations of the basic model with various $\sigma_e^{35}$, and compared $\sigma_e$ at a depth of 12.5 km, $\sigma_e^{12.5}$, as a representative location of shallow slow earthquakes. As in Figure 4, $\alpha^0$ is set at zero, and the $q^0$ values that yield the $\sigma_e^{35}$ values of 50, 55, …, 95, and 100 MPa were determined by the bisection method (Figure S9 in Supporting Information S1). Note that $\sigma_e^{35}$ is not the boundary condition for performing numerical integration of a series of ordinary differential Equations 17–26. Figure 5a shows the $\sigma_e$ distribution for the three cases of no subduction, no reaction, and the basic model with $\sigma_e^{35}$ of 100 MPa. Note that the $q^0$ values of these solutions differ from each other. As long as examined in the present study, the $\sigma_e$ distributions do not exhibit a negative peak above or near the depth of 12.5 km but show a monotonic increase with the increase in depth. The differences in $\sigma_e^{12.5}$, $\Delta\sigma_e^{12.5}$, between the no-subduction and no-reaction cases and between the no-reaction case and the basic model, which represent the mechanical effect of subduction and the effect of smectite dehydration, respectively, are shown in Figure 5b as a function of $\sigma_e^{35}$. Although both effects on $\sigma_e^{12.5}$ become more significant with the increase in $\sigma_e^{35}$, the mechanical effect is always superior to the effect of smectite dehydration in the examined parameter range. However, a negative peak of $\sigma_e$ is absent for any cases (Figure 5a and Figure S8 in Supporting Information S1), clearly indicating that the local $\sigma_e$ around the source region of shallow slow earthquakes, which are typically located at depths shallower than 10–15 km in the Nankai Trough (Nishikawa et al., 2019), is hardly affected by the dehydrated water from smectite particles, as well as by the mechanical effect. When a source term of fluid mass that considers the existence of a splay fault exists, $\sigma_e$ decreases at all depths below the branching area at a depth of approximately 5–8 km, and a locally low $\sigma_e$ is absent as in the basic model (Figure 4a). When considering the local decrease in $k$, a local decrease in $\sigma_e$ is realized around the impermeable zone (set at a depth of 10–15 km) when its effect is significant (Figure 4b). Based on these facts, we conclude that the local decrease in $\sigma_e$ around a certain depth range can be realized by the local decrease in $k$ there.

Liu and Rice (2009) numerically reproduced the total displacement and recurrence interval of deep slow slip events in northern Cascadia with typical rate- and state-dependent friction parameters and suggested a locally very small $\sigma_e$ of a few MPas. Whether shallow slow earthquakes require such a small $\sigma_e$ is an important open question. If so, the occurrence of shallow slow earthquakes is likely to be a result of the processes that cause the local reduction in $k$ around the source region.

### 4.5. Further Refinement of Our Models

#### 4.5.1. Possible Factors Influencing Fluid Source Term

In our formulation, the reaction kinetics of smectite dehydration depend only on $T$ (Huang et al., 1993; Equation 15). However, the interlayer water of smectite particles can be expelled in response to an increase in $\sigma_e$ as well as an increase in $T$ (e.g., Fitts & Brown, 1999). This process affects the distribution of $\omega_{sm}$. Employing reaction kinetics other than that of Huang et al. (1993) (e.g., Pytte & Reynolds, 1989) also affects its distribution. However, these factors do not change the net amount of fluid mass released by smectite dehydration. The present study shows that the effect of the dehydration reaction is rather minor in the shallow portion; therefore, those modifications to the reaction kinetics most likely affect $\sigma_e$ only modestly.

In certain subduction zones where the incoming sediments are rich in amorphous silica, such as the Japan Trench (e.g., Kimura et al., 2012) and the Sumatra subduction margin (e.g., Hüpers et al., 2017), the transition of amorphous silica to quartz via opal-CT can be essential to elucidating the fluid behavior. The source of fluid mass attributed to this series of reactions is located at a shallower portion compared to smectite dehydration (e.g., Kimura et al., 2012), owing to the lower activation energies of the former (approximately 60–70 kJ mol$^{-1}$ according to Mizutani, 1970) than that of the latter (approximately 120 kJ mol$^{-1}$, see Table 1). The strength of the source of fluid mass due to the dehydration of amorphous silica depends on the mineral composition of the subducting sediments. However, in subduction zones with a thick sedimentary layer, the transition of amorphous silica is probably completed before subduction (e.g., Hüpers et al., 2017) and should have no effect on $\sigma_e$.

#### 4.5.2. Fluid Permeation Through Overriding Crust

The basic model and model accounting for local permeability reduction in this study assume that fluid flows only along the subduction channel. However, certain previous studies of two-dimensional hydraulic modeling have suggested that approximately one-third of the fluid can be discharged through the overriding crust (e.g., Lauer & Saffer, 2012; Spinelli et al., 2006). This effect may be modeled in the present framework by introducing a new sink term of fluid mass representing the leakage of the fluid into the overriding crust if a reasonable assumption on its distribution can be made. Tsuji et al. (2014) suggested that excess high $p$ in the subducting sediments is substantially more significant than in the overriding crust at $z > 20$ km except in the branching area, which supports the dominance of the subduction channel in this region.

#### 4.5.3. Complex Stress State in Subduction Zones

Although our models assumed that $\sigma$ is equivalent to the lithostatic pressure as in R1992, complex stress state in subduction zones may violate this approximation. For example, subduction of a seamount can cause locally high (low) $\sigma$ around the leading (trailing) edge (Sun et al., 2020). Tectonic stress in subduction zones can rotate the direction of the maximum principal stress with depth (e.g., van Zelst et al., 2022). More realistic modeling may be possible in the present formulation, if a reasonable expression for $\sigma$ in Equation 17 can be given. However, since the quantitative effects of these factors on $\sigma$ are likely to vary in each subduction zone, a careful consideration focusing on a region of interest is required to properly model the $\sigma$ distribution.

#### 4.5.4. Permeability Model

As concluded in Section 4.4, the local decrease in $k$ may be a key factor in the generation process of shallow slow earthquakes. Potential mechanisms include silica cementation and permeability changes owing to secondary consolidation and fracture. Silica cementation, which was sometimes mentioned in the previous section, has been suggested as a potential cause for the occurrence of deep slow earthquakes (e.g., Audet & Bürgmann, 2014; Gosselin et al., 2020). Furthermore, smectite dehydration releases silica into the pore fluid (Boles & Franks, 1979; Equation 13), possibly promoting permeability reduction around the peak location of the reaction (Figure S2 in Supporting Information S1). Although our model accounting for local permeability reduction employed a boxcar-like function to represent the impermeable zone (Equation 32 and Figure S1c in Supporting Information S1), the shape and intensity of this effect may be modified by considering the kinetics of silica dissolution and precipitation and subsequent crack-seal process.

Since Tanikawa et al. (2014) and Kitajima and Saffer (2014) did not experimentally investigate time-dependent changes in $k$, our basic model and model accounting for splay faults also ignore the effect of time-dependent secondary consolidation. If we consider this process in our models, $k$ at all depths other than the trench is lowered relative to the values expected from a single exponential function of $\sigma_e$. On the other hand, $k$ can increase by the

generation of fractures (fracture permeability). Laboratory experiments (e.g., Griffith et al., 2009) and theoretical and numerical studies (e.g., Poliakov et al., 2002) demonstrated the growth of cracks off the main fault owing to dynamic rupture propagation during seismic events. Whether slow earthquakes have a similar effect on $k$ is still unclear and should be addressed in the future study. If the events with slower slip rates cause less increase in $k$, the source region of shallow slow earthquakes may be less permeable relative to the deeper seismogenic portion. Combination of these two effects on $k$ (i.e., secondary consolidation and fracture permeability) may result in the local decrease in $k$ only within the region shallower than the seismogenic zone, as assumed in our model accounting for local permeability reduction (Figure 4b).

### 4.5.5. Transient Behavior

Although we focused on the steady-state solution as in previous hydraulic modeling (e.g., Bekins et al., 1995; Bethke, 1986; Ellis et al., 2015; Lauer & Saffer, 2012, 2015; Rice, 1992; Saffer & Bekins, 1998; Spinelli et al., 2006; Sun et al., 2020), transient behavior is expected in subduction zones. For instance, temporal changes in flow rates have been observed in boreholes (Hirose et al., 2021; Solomon et al., 2009). Transient fault slip most likely perturbs the hydraulic properties of the fault zone (e.g., Sibson, 1992), as demonstrated by friction experiments and permeability measurements using the Nankai sediments (e.g., Ikari & Saffer, 2012; Tanikawa et al., 2012). Silica cementation and secondary consolidation can also affect the hydraulic properties of the fault zone over time (e.g., Chester & Logan, 1986). Incorporating these time dependencies is beyond the scope of the present study but warrants further study.

We first formulated a set of partial differential equations with respect to $t$ and $z$ and then used the steady-state assumption ($\partial/\partial t = 0$) to obtain the system of equations solved in the present study (e.g., Equations 17–26). In principle, the simulation of certain transient behaviors is possible, such as the migration of higher $p$ than the steady-state solution. Coupling with the fault motion requires substantially more sophisticated models of $V$, $V_{\mathrm{f}}$, and $k$ for rocks along the subduction channel and within the overriding crust that experience a vastly wide range of mechanical and chemical conditions at various timescales (e.g., coseismic damage and fracture permeability, time-dependent compaction associated with healing of the fault, effect of aseismic shear deformation, and transport and precipitation of silica). Steady-state solutions such as those obtained in this study may be useful in such studies, providing initial conditions or reference states to which the time-dependent solutions are compared, as in previous studies (e.g., Bekins et al., 1995; Spinelli et al., 2006).

## 5. Conclusions

In this study, we developed hydraulic models of a subduction channel based on the model in Rice (1992), considering the effect of smectite dehydration and the mechanical effect of subduction of sediments and realistic fluid properties. By using typical geometrical and hydraulic properties for the Kumano transect in the Nankai Trough as a representative subduction zone, we obtained distributions of effective normal stress, $\sigma_{\mathrm{e}}$, as a function of the volumetric fluid flux at trench $q^0$ and the composition of the subducting sediments for this basic model. By modifying the basic model, we investigated the effects of fluid leakage through a splay fault and local permeability reduction. We drew the following conclusions from the study results:

1. A physically sound solution of non-negative $\sigma_{\mathrm{e}}$ in the basic model exists only within a restricted range of $q^0$, and this range is consistent with observations of the flow rate in subduction zones.
2. The gradient of $\sigma_{\mathrm{e}}$ in the basic model decreased remarkably with the increase in depth, as reported by Rice (1992). However, the asymptotic behavior in the solution reported by Rice (1992) was not realized because of the implementation of realistic fluid properties. The increase in $\sigma_{\mathrm{e}}$ suggests a weak depth-dependent stress drop of earthquakes, whose evaluation may be complicated by the scatter in the stress drop data.
3. The mechanical effect of subduction is always a source of pore-fluid pressure $p$, whereas the effect of smectite dehydration can either be its sink or source depending on the boundary conditions at the trench. The existence of a splay fault always works as a sink term of $p$, which decreases $\sigma_{\mathrm{e}}$ below the branching area if the boundary condition at the trench is fixed. Local reduction in permeability also increased $p$ and thus decreased $\sigma_{\mathrm{e}}$, but its effect was spatially restricted only around the impermeable zone.
4. The obtained distribution of $\sigma_{\mathrm{e}}$ can be used as a boundary condition for more realistic earthquake cycle simulations than those based on the solution reported by Rice (1992). Although the difference obtained when using the basic model would only be modest, the other models studied here would impact the resultant fault motion during seismic cycles.

5. We failed to obtain a solution with a negative peak of $\sigma_e$ at approximately or above the peak depth of the dehydration reaction in the basic model, which is sometimes considered to be responsible for the generation of slow earthquakes. A locally low $\sigma_e$ is also absent when a splay fault is considered. If we consider a local decrease in permeability, which can be caused by the clogging process of conduits, then locally low $\sigma_e$ is realized, potentially allowing for the occurrence of shallow slow earthquakes.

## Conflict of Interest

The authors declare no conflicts of interest relevant to this study.

## Data Availability Statement

All the codes used for the numerical calculations are available at Zenodo (https://doi.org/10.5281/zenodo.7113110). The complete data set generated using the codes used in this study is available at Zenodo (https://doi.org/10.5281/zenodo.7113116, https://doi.org/10.5281/zenodo.7113149, and https://doi.org/10.5281/zenodo.7113178 for the basic model, https://doi.org/10.5281/zenodo.7113171 for the model with a splay fault, and https://doi.org/10.5281/zenodo.7113154 for the model with local permeability reduction). Figures were created using the open-source Python function matplotlib.pyplot (Matplotlib v3.4.2) and Adobe Illustrator (https://www.adobe.com/products/illustrator.html).

## References

Allmann, B. P., & Shearer, P. M. (2009). Global variations of stress drop for moderate to large earthquakes. *Journal of Geophysical Research*, *114*(B1), B01310. https://doi.org/10.1029/2008JB005821

Athy, L. F. (1930). Density, porosity, and compaction of sedimentary rocks. *AAPG Bulletin*, *14*(1), 194–200. https://doi.org/10.1306/3d93289e-16b1-11d7-8645000102c1865d

Audet, P., & Bürgmann, R. (2014). Possible control of subduction zone slow-earthquake periodicity by silica enrichment. *Nature*, *510*(7505), 389–392. https://doi.org/10.1038/nature13391

Bekins, B. A., Mccaffrey, A. M., & Dreiss, S. J. (1995). Episodic and constant flow models for the origin of low-chloride waters in a modern accretionary complex. *Water Resources Research*, *31*(12), 3205–3215. https://doi.org/10.1029/95WR02569

Beroza, G. C., & Ide, S. (2011). Slow earthquakes and nonvolcanic tremor. *Annual Review of Earth and Planetary Sciences*, *39*(1), 271–296. https://doi.org/10.1146/annurev-earth-040809-152531

Bethke, C. M. (1986). Inverse hydrologic analysis of the distribution and origin of gulf coast-type geopressured zones. *Journal of Geophysical Research*, *91*(B6), 6535–6545. https://doi.org/10.31866/2410-1176.35.2016.158254

Bird, P. (1984). Hydration-phase diagrams and friction of montmorillonite under laboratory and geologic conditions, with implications for shale compaction, slope stability, and strength of fault gouge. *Tectonophysics*, *107*(3–4), 235–260. https://doi.org/10.1016/0040-1951(84)90253-1

Blanpied, M. L., Lockner, D. A., & Byerlee, J. D. (1991). Fault stability inferred from granite sliding experiments at hydrothermal conditions. *Geophysical Research Letters*, *18*(4), 609–612. https://doi.org/10.1029/91GL00469

Boles, J. R., & Franks, S. G. (1979). Clay diagenesis in Wilcox sandstones of southwest Texas: Implications of smectite diagenesis on sandstone cementation. *Journal of Sedimentary Petrology*, *49*(1), 55–70. https://doi.org/10.1306/212F76BC-2B24-11D7-8648000102C1865D

Broberg, K. B. (1978). On transient sliding motion. *Geophysical Journal of the Royal Astronomical Society*, *52*(3), 397–432. https://doi.org/10.1111/j.1365-246X.1978.tb04240.x

Byerlee, J. (1978). Friction of rocks. *Pure and Applied Geophysics*, *116*(4–5), 615–626. https://doi.org/10.1007/bf00876528

Chester, F. M., & Logan, J. M. (1986). Implications for mechanical properties of brittle faults from observations of the Punchbowl fault zone, California. *Pure and Applied Geophysics*, *124*(1–2), 79–106. https://doi.org/10.1007/BF00875720

Dieterich, J. H. (1979). Modeling of rock friction 1. Experimental results and constitutive equations. *Journal of Geophysical Research*, *84*(B5), 2161–2168. https://doi.org/10.1029/JB084iB05p02161

Ellis, S., Fagereng, Å., Barker, D., Henrys, S., Saffer, D., Wallace, L., et al. (2015). Fluid budgets along the northern Hikurangi subduction margin, New Zealand: The effect of a subducting seamount on fluid pressure. *Geophysical Journal International*, *202*(1), 277–297. https://doi.org/10.1093/gji/ggv127

Expedition 316 Scientists. (2009). Expedition 316 site C0007. In M. Kinoshita, H. Tobin, J. Ashi, G. Kimura, S. Lallemant, E. J. Screaton, et al. (Eds.), *Proceedings of the Integrated Ocean Drilling Program* (Vol. 314/315/316). Integrated Ocean Drilling Program Management International, Inc. https://doi.org/10.2204/iodp.proc.314315316.135.2009

Expedition 322 Scientists. (2010). Site C0011. In S. Saito, M. B. Underwood, Y. Kubo, & the Expedition 322 Scientists. (Eds.), *Proceedings of the Integrated Ocean Drilling Program* (Vol. 322). Integrated Ocean Drilling Program Management International, Inc. https://doi.org/10.2204/iodp.proc.322.103.2010

Fitts, T. G., & Brown, K. M. (1999). Stress-induced smectite dehydration: Ramifications for patterns of freshening and fluid expulsion in the N. Barbados accretionary wedge. *Earth and Planetary Science Letters*, *172*(1–2), 179–197. https://doi.org/10.1016/S0012-821X(99)00168-5

Freed, R. L., & Peacor, D. R. (1989). Variability in temperature of the smectite/illite reaction in Gulf Coast sediments. *Clay Minerals*, *24*(2), 171–180. https://doi.org/10.1180/claymin.1989.024.2.05

Fulton, P. M., Saffer, D. M., & Bekins, B. A. (2009). A critical evaluation of crustal dehydration as the cause of an overpressured and weak San Andreas Fault. *Earth and Planetary Science Letters*, *284*(3–4), 447–454. https://doi.org/10.1016/j.epsl.2009.05.009

Gosselin, J. M., Audet, P., Estève, C., McLellan, M., Mosher, S. G., & Schaeffer, A. J. (2020). Seismic evidence for megathrust fault-valve behavior during episodic tremor and slip. *Science Advances*, *6*(4), eaay5174. https://doi.org/10.1126/sciadv.aay5174

Griffith, W. A., Rosakis, A., Pollard, D. D., & Ko, C. W. (2009). Dynamic rupture experiments elucidate tensile crack development during propagating earthquake ruptures. *Geology*, *37*(9), 795–798. https://doi.org/10.1130/G30064A.1

Guo, J., & Underwood, M. B. (2012). Data report: Clay mineral assemblages from the Nankai Trough accretionary prism and the Kumano basin, IODP expeditions 315 and 316, NanTroSEIZE stage 1. In M. Kinoshita, H. Tobin, J. Ashi, G. Kimura, S. Lallemant, E. J. Screaton, et al. (Eds.), *Proceedings of the Integrated Ocean Drilling Program* (Vol. 314/315/316). Integrated Ocean Drilling Program Management International, Inc. https://doi.org/10.2204/iodp.proc.314315316.202.2012

Hirose, H., Hirahara, K., Kimata, F., Fujii, N., & Miyazaki, S. (1999). A slow thrust slip event following the two 1996 Hyuganada earthquakes beneath the Bungo Channel, southwest Japan. *Geophysical Research Letters*, *26*(21), 3237–3240. https://doi.org/10.1029/1999GL010999

Hirose, T., Hamada, Y., Tanikawa, W., Kamiya, N., Yamamoto, Y., Tsuji, T., et al. (2021). High fluid-pressure patches beneath the décollement: A potential source of slow earthquakes in the Nankai Trough off cape Muroto. *Journal of Geophysical Research: Solid Earth*, *126*(6), e2021JB021831. https://doi.org/10.1029/2021JB021831

Huang, W.-L., Longo, J. M., & Pevear, D. R. (1993). An experimentally derived kinetic model for smectite-to-illite conversion and its use as a geothermometer. *Clays and Clay Minerals*, *41*(2), 162–177. https://doi.org/10.1346/CCMN.1993.0410205

Hunziker, J. C. (1986). The evolution of illite to muscovite: An example of the behaviour of isotopes in low-grade metamorphic terrains. *Chemical Geology*, *57*(1–2), 31–40. https://doi.org/10.1016/0009-2541(86)90092-6

Hüpers, A., Torres, M. E., Owari, S., McNeill, L. C., Dugan, B., Henstock, T. J., et al. (2017). Release of mineral-bound water prior to subduction tied to shallow seismogenic slip off Sumatra. *Science*, *356*(6340), 841–844. https://doi.org/10.1126/science.aal3429

Hyndman, R. D., McCrory, P. A., Wech, A., Kao, H., & Ague, J. (2015). Cascadia subducting plate fluids channelled to fore-arc mantle corner: ETS and silica deposition. *Journal of Geophysical Research: Solid Earth*, *120*(6), 4344–4358. https://doi.org/10.1002/2015JB011920

Hyndman, R. D., & Peacock, S. M. (2003). Serpentinization of the forearc mantle. *Earth and Planetary Science Letters*, *212*(3–4), 417–432. https://doi.org/10.1016/S0012-821X(03)00263-2

Hyndman, R. D., Yamano, M., & Oleskevich, D. A. (1997). The seismogenic zone of subduction thrust faults. *Island Arc*, 6(3), 244–260. https://doi.org/10.1111/j.1440-1738.1997.tb00175.x

Ikari, M. J., & Saffer, D. M. (2012). Permeability contrasts between sheared and normally consolidated sediments in the Nankai accretionary prism. *Marine Geology*, *295–298*, 1–13. https://doi.org/10.1016/j.margeo.2011.11.006

Kameda, J., Ujiie, K., Yamaguchi, A., & Kimura, G. (2011). Smectite to chlorite conversion by frictional heating along a subduction thrust. *Earth and Planetary Science Letters*, *305*(1–2), 161–170. https://doi.org/10.1016/j.epsl.2011.02.051

Kimura, G., Hina, S., Hamada, Y., Kameda, J., Tsuji, T., Kinoshita, M., & Yamaguchi, A. (2012). Runaway slip to the trench due to rupture of highly pressurized megathrust beneath the middle trench slope: The tsunami genesis of the 2011 Tohoku earthquake off the east coast of northern Japan. *Earth and Planetary Science Letters*, *339*(340), 32–45. https://doi.org/10.1016/j.epsl.2012.04.002

Kitajima, H., & Saffer, D. M. (2014). Consolidation state of incoming sediments to the Nankai Trough subduction zone: Implications for sediment deformation. *Geochemistry, Geophysics, Geosystems*, *15*(7), 2821–2839. https://doi.org/10.1002/2014GC005360

Kodaira, S., Iidaka, T., Kato, A., Park, J.-O., Iwasaki, T., & Kaneda, Y. (2004). High pore fluid pressure may cause silent slip in the Nankai Trough. *Science*, *304*(5675), 1295–1298. https://doi.org/10.1126/science.1096535

Lapusta, N., Rice, J. R., Ben-Zion, Y., & Zheng, G. (2000). Elastodynamic analysis for slow tectonic loading with spontaneous rupture episodes on faults with rate- and state-dependent friction. *Journal of Geophysical Research*, *105*(B10), 23765–23789. https://doi.org/10.1029/2000jb900250

Lauer, R. M., & Saffer, D. M. (2012). Fluid budgets of subduction zone forearcs: The contribution of splay faults. *Geophysical Research Letters*, *39*(13), L13604. https://doi.org/10.1029/2012GL052182

Lauer, R. M., & Saffer, D. M. (2015). The imcat of splay faults on fluid flow, solute transport, and pore pressure distribution in subduction zones: A case study offshore the Nicoya Peninsla, Costa Rica. *Geochemistry, Geophysics, Geosystems*, *16*(4), 1089–1104. https://doi.org/10.1002/2014GC005638

Liu, Y., & Rice, J. R. (2005). Aseismic slip transients emerge spontaneously in three-dimensional rate and state modeling of subduction earthquake sequences. *Journal of Geophysical Research*, *110*(B8), B08307. https://doi.org/10.1029/2004JB003424

Liu, Y., & Rice, J. R. (2007). Spontaneous and triggered aseismic deformation transients in a subduction fault model. *Journal of Geophysical Research*, *112*(B9), B09404. https://doi.org/10.1029/2007JB004930

Liu, Y., & Rice, J. R. (2009). Slow slip predictions based on granite and gabbro friction data compared to GPS measurements in northern Cascadia. *Journal of Geophysical Research*, *114*(B9), B09407. https://doi.org/10.1029/2008JB006142

Marcaillou, B., Henry, P., Kinoshita, M., Kanamatsu, T., Screaton, E., Daigle, H., et al. (2012). Seismogenic zone temperatures and heat-flow anomalies in the To-nankai margin segment based on temperature data from IODP expedition 333 and thermal model. *Earth and Planetary Science Letters*, *349*(350), 171–185. https://doi.org/10.1016/j.epsl.2012.06.048

Mizutani, S. (1970). Silica minerals in the early stage of diagenesis. *Sedimentology*, *15*(3–4), 419–436. https://doi.org/10.1111/j.1365-3091.1970.tb02193.x

Moore, G. F., Park, J.-O., Bangs, N. L., Gulick, S. P., Tobin, H., Nakamura, Y., et al. (2009). Structural and seismic stratigraphic framework of the NanTroSEIZE Stage 1 transect. In M. Kinoshita, H. Tobin, J. Ashi, G. Kimura, S. Lallemant, E. J. Screaton, et al. (Eds.), *Proceedings of the Integrated Ocean Drilling Program*. Integrated Ocean Drilling Program Management International, Inc. https://doi.org/10.2204/iodp.proc.314315316.102.2009

Nakanishi, A., Park, J.-O., Miura, S., Kodaira, S., Kaneda, Y., Takahashi, N., et al. (2002). Crustal structure across the coseismic rupture zone of the 1944 Tonankai earthquake, the central Nankai Trough seismogenic zone. *Journal of Geophysical Research*, *107*(B1), EPM2-1–EPM2-21. https://doi.org/10.1029/2003jb002576

Nishikawa, T., Matsuzawa, T., Ohta, K., Uchida, N., Nishimura, T., & Ide, S. (2019). The slow earthquake spectrum in the Japan Trench illuminated by the S-net seafloor observatories. *Science*, *365*(6455), 808–813. https://doi.org/10.1126/science.aax5618

Obara, K. (2002). Nonvolcanic deep tremor associated with subduction in southwest Japan. *Science*, *296*(5573), 1679–1681. https://doi.org/10.1126/science.1070378

Obara, K., & Kato, A. (2016). Connecting slow earthquakes to huge earthquakes. *Science*, *353*(6296), 253–257. https://doi.org/10.1126/science.aaf1512

Outerbridge, K. C., Dixon, T. H., Schwartz, S. Y., Walter, J. I., Protti, M., Gonzalez, V., et al. (2010). A tremor and slip event on the Cocos-Caribbean subduction zone as measured by a global positioning system (GPS) and seismic network on the Nicoya Peninsula, Costa Rica. *Journal of Geophysical Research*, *115*(B10), B10408. https://doi.org/10.1029/2009JB006845

Peacock, S. M. (2009). Thermal and metamorphic environment of subduction zone episodic tremor and slip. *Journal of Geophysical Research*, *114*, B00A07. https://doi.org/10.1029/2008JB005978

Poliakov, A. N. B., Dmowska, R., & Rice, J. R. (2002). Dynamic shear rupture interactions with fault bends and off-axis secondary faulting. *Journal of Geophysical Research*, *107*(B11), ESE6-1–ESE6-18. https://doi.org/10.1029/2001jb000572

Pytte, A. M., & Reynolds, R. C. (1989). The thermal transformation of smectite to illite. In N. D. Naeser & T. H. McCulloh (Eds.), *Thermal history of sedimentary basins* (pp. 133–140). Springer. https://doi.org/10.1007/978-1-4612-3492-0_8

Rice, J. R. (1992). Fault stress states, pore pressure distributions, and the weakness of the San Andreas Fault. In B. Evans & T. Wong (Eds.), *Fault mechanics and transport properties of rocks* (pp. 475–503). Elsevier. https://doi.org/10.1016/S0074-6142(08)62835-1

Rimstidt, J. D., & Barnes, H. L. (1980). The kinetics of silica-water reactions. *Geochimica et Cosmochimica Acta*, *44*(11), 1683–1699. https://doi.org/10.1016/0016-7037(80)90220-3

Rogers, G., & Dragert, H. (2003). Episodic tremor and slip on the Cascadia subduction zone: The chatter of silent slip. *Science*, *300*(5627), 1942–1943. https://doi.org/10.1126/science.1084783

Ruina, A. (1983). Slip instability and state variable friction laws. *Journal of Geophysical Research*, *88*(B12), 10359–10370. https://doi.org/10.1029/JB088iB12p10359

Saffer, D. M., & Bekins, B. A. (1998). Episodic fluid flow in the Nankai accretionary complex: Timescale, geochemistry, flow rates, and fluid budget. *Journal of Geophysical Research*, *103*(B12), 30351–30370. https://doi.org/10.1029/98JB01983

Saffer, D. M., & Wallace, L. M. (2015). The frictional, hydrologic, metamorphic and thermal habitat of shallow slow earthquakes. *Nature Geoscience*, *8*, 594–600. https://doi.org/10.1038/ngeo2490

Schön, J. H. (2015). *Physical properties of rocks: Fundamentals and principles of petrophysics* (3rd ed.). Elsevier.

Seno, T., Stein, S., & Gripp, A. E. (1993). A model for the motion of the Philippine Sea Plate consistent with NUVEL-1 and geological data. *Journal of Geophysical Research*, *98*(B10), 17941–17948. https://doi.org/10.1029/93jb00782

Shelly, D. R., Beroza, G. C., Ide, S., & Nakamula, S. (2006). Low-frequency earthquakes in Shikoku, Japan, and their relationship to episodic tremor and slip. *Nature*, *442*(7099), 188–191. https://doi.org/10.1038/nature04931

Sibson, R. H. (1992). Implications of fault-valve behaviour for rupture nucleation and recurrence. *Tectonophysics*, *211*(1–4), 283–293. https://doi.org/10.1016/0040-1951(92)90065-E

Solomon, E. A., Kastner, M., Wheat, C. G., Jannasch, H., Robertson, G., Davis, E. E., & Morris, J. D. (2009). Long-term hydrochemical records in the oceanic basement and forearc prism at the Costa Rica subduction zone. *Earth and Planetary Science Letters*, *282*(1–4), 240–251. https://doi.org/10.1016/j.epsl.2009.03.022

Song, T. A., Helmberger, D. V., Brudzinski, M. R., Clayton, R. W., Davis, P., Pérez-campos, X., & Singh, S. K. (2009). Subducting slab ultra-slow velocity layer coincident with silent earthquakes in southern Mexico. *Science*, *324*(5926), 502–507. https://doi.org/10.1126/science.1167595

Spinelli, G. A., & Hutton, A., & the Expedition 322 Scientists. (2013). Data report: Amorphous silica content of sediment from sites C0011 and C0012 in the Shikoku basin on the NanTroSEIZE transect. In S. Saito, M. B. Underwood, & Y. Kubo (Eds.), *Proceedings of the Integrated Ocean Drilling Program* (Vol. 322). Integrated Ocean Drilling Program Management International, Inc. https://doi.org/10.2204/iodp.proc.322.204.2013

Spinelli, G. A., Saffer, D. M., & Underwood, M. B. (2006). Hydrogeologic responses to three-dimensional temperature variability, Costa Rica subduction margin. *Journal of Geophysical Research*, *111*(B4), B04403. https://doi.org/10.1029/2004JB003436

Sun, T., Saffer, D., & Ellis, S. (2020). Mechanical and hydrological effects of seamount subduction on megathrust stress and slip. *Nature Geoscience*, *13*(3), 249–255. https://doi.org/10.1038/s41561-020-0542-0

Suppe, J., & Wittke, J. H. (1977). Abnormal pore-fluid pressures in relation to stratigraphy and structure in the active fold-and-thrust belt of Northwestern Taiwan. *Petroleum Geology of Taiwan*, *14*, 11–24.

Tanikawa, W., Mukoyoshi, H., Lin, W., Hirose, T., & Tsutsumi, A. (2014). Pressure dependence of fluid transport properties of shallow fault systems in the Nankai subduction zone. *Earth Planets and Space*, *66*(1), 90. https://doi.org/10.1186/1880-5981-66-90

Tanikawa, W., Mukoyoshi, H., Tadai, O., Hirose, T., Tsutsumi, A., & Lin, W. (2012). Velocity dependence of shear-induced permeability associated with frictional behavior in fault zones of the Nankai subduction zone. *Journal of Geophysical Research*, *117*(B5), B05405. https://doi.org/10.1029/2011JB008956

Townend, J., & Zoback, M. D. (2000). How faulting keeps the crust strong. *Geology*, *28*(5), 399–402. https://doi.org/10.1130/0091-7613(2000)028<0399:HFKTCS>2.3.CO;2

Tsuji, T., Kamei, R., & Pratt, R. G. (2014). Pore pressure distribution of a mega-splay fault system in the Nankai trough subduction zone: Insight into up-dip extent of the seismogenic zone. *Earth and Planetary Science Letters*, *396*, 165–178. https://doi.org/10.1016/j.epsl.2014.04.011

Underwood, M. B., & Guo, J., & the Expedition 322 Scientists. (2013). Data report: Clay mineral assemblages in the Shikoku basin, NanTroSEIZE subduction inputs, IODP sites C0011 and C0012. In S. Saito, M. B. Underwood, & Y. Kubo (Eds.), *Proceedings of the Integrated Ocean Drilling Program* (Vol. 322). Integrated Ocean Drilling Program Management International, Inc. https://doi.org/10.2204/iodp.proc.322.202.2013

van Dinther, Y., Gerya, T. V., Dalguer, L. A., Mai, P. M., Morra, G., & Giardini, D. (2013). The seismic cycle at subduction thrusts: Insights from seismo-thermo- mechanical models. *Journal of Geophysical Research: Solid Earth*, *118*(12), 6183–6202. https://doi.org/10.1002/2013JB010380

van Zelst, I., Rannabauer, L., Gabriel, A.-A., & van Dinther, Y. (2022). Earthquake rupture on multiple splay faults and its effect on tsunamis. *Journal of Geophysical Research: Solid Earth*, *127*(8), e2022JB024300. https://doi.org/10.1029/2022jb024300

Voss, C. I. (1984). *A finite-element simulation model for saturated-unsaturated, fluid-density-dependent groundwater flow with energy transport or chemically-reactive single-species solute transport* (Vol. 409). U.S. Geological Survey.

Wagner, W., & Pruß, A. (2002). The IAPWS formulation 1995 for the thermodynamic properties of ordinary water substance for general and scientific use. *Journal of Physical and Chemical Reference Data*, *31*(2), 387–535. https://doi.org/10.1063/1.1461829

Wallace, L. M., & Beavan, J. (2010). Diverse slow slip behavior at the Hikurangi subduction margin, New Zealand. *Journal of Geophysical Research*, *115*(B12), B12402. https://doi.org/10.1029/2010JB007717